



저작자표시-비영리-변경금지 2.0 대한민국

이용자는 아래의 조건을 따르는 경우에 한하여 자유롭게

- 이 저작물을 복제, 배포, 전송, 전시, 공연 및 방송할 수 있습니다.

다음과 같은 조건을 따라야 합니다:



저작자표시. 귀하는 원저작자를 표시하여야 합니다.



비영리. 귀하는 이 저작물을 영리 목적으로 이용할 수 없습니다.



변경금지. 귀하는 이 저작물을 개작, 변형 또는 가공할 수 없습니다.

- 귀하는, 이 저작물의 재이용이나 배포의 경우, 이 저작물에 적용된 이용허락조건을 명확하게 나타내어야 합니다.
- 저작권자로부터 별도의 허가를 받으면 이러한 조건들은 적용되지 않습니다.

저작권법에 따른 이용자의 권리는 위의 내용에 의하여 영향을 받지 않습니다.

이것은 [이용허락규약\(Legal Code\)](#)을 이해하기 쉽게 요약한 것입니다.

[Disclaimer](#)

Master's Thesis

Generation of Windowed Multipole Library for on-
the-fly Doppler Broadening in UNIST In-house
Monte Carlo Code

Azamat Khassenov

Department of Nuclear Engineering

Graduate School of UNIST

2018

Generation of Windowed Multipole Library for on- the-fly Doppler Broadening in UNIST In-house Monte Carlo Code

Azamat Khassenov

Department of Nuclear Engineering

Graduate School of UNIST

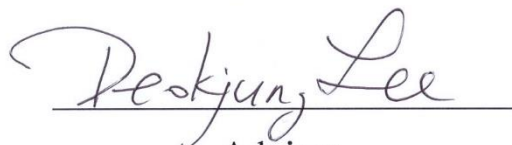
Generation of Windowed Multipole Library for on- the-fly Doppler Broadening in UNIST In-house Monte Carlo Code

A thesis/dissertation
submitted to the Graduate School of UNIST
in partial fulfillment of the
requirements for the degree of
Master of Science

Azamat Khassenov

6. 15. 2018

Approved by



Advisor

Deokjung Lee

Generation of Windowed Multipole Library for on- the-fly Doppler Broadening in UNIST In-house Monte Carlo Code

Azamat Khassenov

This certifies that the thesis/dissertation of Azamat Khassenov is approved.

6. 15. 2018



Advisor: Professor Deokjung Lee



Professor Hyun Chul Lee



Professor Eisung Yoon

Abstract

This thesis presents the generation and application results of the windowed multipole (WMP) library in UNIST in-house Monte Carlo code (MCS). The given library is used in the on-the-fly Doppler broadening of microscopic cross section at the temperature of the interest during a Monte Carlo simulation. This feature is one of the major requirements for multi-physics simulations; in other words, coupled calculations of neutron transport, thermal-hydraulics, and fuel performance codes. A windowed multipole library significantly reduces the memory necessary for cross section storage with a reasonable increase in the total Monte Carlo simulation time. The ENDF/B-VII.1 neutron induced library contains information on 430 isotopes, where 331 contain resonance parameters for the resolved resonance region. In the first step, the parameters from the evaluated nuclear data file were converted into corresponding rigorous multipole parameters, which can be directly used in temperature dependent cross section reconstruction. Further, in order to reduce the cross section generation time the energy window concept was applied with an accuracy threshold of 0.1 % relative difference in comparison to the reference cross section. The accuracy and effect of the generated windowed multipole library on the MCS simulation was evaluated using fresh and burned PWR fuel pins, and assemblies.

Contents

I. Introduction	1
II. Theory.....	2
2.1 R-Matrix Theory	2
2.2 Multipole Representation	5
2.3 Doppler broadening.....	7
III. Converting Resonance Parameters	9
3.1 Breit-Wigner Formalisms	9
3.2 Reich-Moore Formalism	13
IV. Windowed Multipole Representation	21
4.1 Window Concept.....	21
4.2 Polynomial Fitting	23
4.3 Windowed Multipole Library	24
V. Numerical Results	27
5.1 PWR Fuel Pin	27
5.2 PWR Fuel Assembly	38
5.3 Performance Tests	41
VI. Conclusion and Future Work.....	42
APPENDIX A.....	43
APPENDIX B.....	46

List of Figures

Figure 1. Resonance cross section comparison at 0 K and 3000 K temperatures.....	8
Figure 2. Multipole reconstructed cross sections of ^{241}Am at 0 K temperature.	13
Figure 3. Distribution of poles for ^{238}U isotope.	18
Figure 4. $\text{Re}(F(u))$: s-wavelike poles corresponding to the first 10 p-wave resonances of ^{238}U	18
Figure 5. $\text{Im}(F(u))$: s-wavelike poles corresponding to the first 10 p-wave resonances of ^{238}U	19
Figure 6. Not s-wavelike poles clusters along imaginary axis for ^{238}U isotope.	19
Figure 7. Multipole reconstructed cross sections of ^{238}U at 0 K temperature.	20
Figure 8. XS generated by poles corresponding to 6.673491 eV s-wave resonance of ^{238}U	21
Figure 9. Window concept scheme (inner and outer windows).....	22
Figure 10. Windowed multipole library generation algorithm.	24
Figure 11. Window concept applied to ^{241}Am isotope.....	25
Figure 12. Multiplication factor comparison: ACE and WMP w.r.t. burnup for problems 1C, and 1I.28	
Figure 13. Pin 1C absolute and relative differences in number density for fission products.....	29
Figure 14. Pin 1C absolute and relative differences in number density for important actinides.	30
Figure 15. Pin 1I absolute and relative differences in number density for fission products.	30
Figure 16. Pin 1I absolute and relative differences in number density for important actinides.....	31
Figure 17. Difference of k: ACE and WMP w.r.t. temperature at 0.00 and 60.00 MWd/kgHM.....	32
Figure 18. Isotope-wise reactivity error for pin 1C at 0.00 MWd/kgHM.	33
Figure 19. Isotope-wise reactivity error for pin 1C at 60.00 MWd/kgHM.....	33
Figure 20. Isotope-wise reactivity error for pin 1I at 0.00 MWd/kgHM.	33
Figure 21. Isotope-wise reactivity error for pin 1I at 60.00 MWd/kgHM.	34
Figure 22. Isotope-wise reaction rate difference for pin 1C at 0.00 MWd/kgHM.....	34
Figure 23. Isotope-wise reaction rate differences for pin 1C at 60.00 MWd/kgHM.	35
Figure 24. Isotope-wise reaction rate differences for pin 1I at 0.00 MWd/kgHM.	36
Figure 25. Isotope-wise reaction rate differences for pin 1I at 60.00 MWd/kgHM.	37
Figure 26. FA 2C: Relative pin power difference between ACE and WMP.	39
Figure 27. FA 2F: Relative pin power difference between ACE and WMP.....	40
Figure 28. FA 2G: Relative pin power difference between ACE and WMP.....	40
Figure 29. FA 2P: Relative pin power difference between ACE and WMP.....	40

List of Tables

Table 1. Summary on ENDF/B-VII.1 isotopes.....	5
Table 2. Important orbital momentum dependent functions.....	9
Table 3. The first order derivative of $q_l(u)$ function.....	17
Table 4. The 40 step burnup points for depletion calculation.....	27
Table 5. VERA single pin depletion benchmark problems.....	28
Table 6. List of nuclides used for comparison study.	29
Table 7. VERA single fuel assembly depletion benchmark problems.....	38
Table 8. Selected VERA single fuel assembly problems multiplication factor comparison.	39
Table 9. Performance tests: Monte Carlo simulation configurations.....	41
Table 10. Estimated clock cycles per <code>get_xs_micro_all</code> call (* indicates sub-function).....	41
Table 11. Breit-Wigner s-wave resonance parameters.	43
Table 12. Calculated poles and residues for ^{78}Kr isotope.	44
Table 13. Reich-Moore s-wave resonance parameters.	44
Table 14. Calculated poles and residues for ^{241}Pu isotope.....	45
Table 15. List of isotopes with WMP library generated from ENDF/B-VII.1.	46

I. Introduction

Over the last several decades, there has been a growth in interest in high fidelity simulations of the current and future nuclear systems. The multi-physics approach enables the simulation of nuclear systems in detail and in terms of different physics. In other words, the coupling calculation of neutron transport, thermal hydraulics, fuel performance, and nuclear chemistry codes allows to achieve very accurate, detailed predictions of the nuclear reactor behavior. One of the most important parameters to take into account is the temperature of a material, or its distribution within the nuclear reactor core. Conventionally, Monte Carlo code solves the neutron transport problem assuming a constant temperature profile within the same material, which is not true for the operating commercial nuclear power plants. The cross section (XS) - the key quantity required for reactor physics calculations - is very dependent on temperature. The nuclide XS is experimentally measured using various known techniques, and evaluated for further applications in nuclear engineering. The R-Matrix theory allows the reconstruction of the neutron induced resonance cross sections employing the parameters from evaluated nuclear data files (*i.e.*, ENDF-B/VII.1).

The Monte Carlo approach typically employs the continuous energy representation of the neutron XS for all isotopes of interest; hence, several hundreds of thousands of energy points are required. This increases the memory associated with storing the XS during the neutron transport calculation. In order to perform the coupled simulation of the neutron transport and thermal hydraulics codes, which provides temperature feedback, a large number of ACE formatted cross sections at various temperatures need to be pre-generated. In order to overcome the memory burden, various on-the-fly Doppler broadening techniques have been proposed. One of the most promising approaches is windowed multipole representation, proposed by the Computational Reactor Physics Group (CRPG) in MIT. This method of reconstructing a cross section at the target temperature of interest significantly reduces memory consumption from GBs to several tens of MBs. In addition, to decrease the memory requirements associated with XS, windowed multipole representation does not significantly increase the overall Monte Carlo simulation time.

In this document, the generation of a windowed multipole library for the on-the-fly Doppler broadening routine in UNIST in-house Monte Carlo code MCS is discussed, and its further verification results for fuel pin and assembly problems are provided. The starting point is to obtain the parameters (poles and residues) from the resonance parameters given in the evaluated nuclear data base. Next, following the MIT optimization technique, also known as window concept, an efficient windowed multipole library for every possible isotope is generated.

II. Theory

The theory behind the reconstruction of the resolved resonance region microscopic cross section is described in Section 2.1, including a summary of the conventional formalisms. In Section 2.2, the rigorous multipole representation is summarized. Doppler broadening techniques of the cross section and the major drawbacks are described Section 2.3.

2.1 R-Matrix Theory

The general R-Matrix theory was introduced by Wigner and Eisenbud [1]. It considers the nucleon-nucleus interaction and predicts the experimental behavior of the microscopic cross sections. This theory does not require the internal structure information of the nucleus; the parameters or elements of the R matrix used to reconstruct resonance cross sections are determined by evaluation of the measured data. A detailed description of the R-Matrix theory was provided by Lane and Thomas [2].

This section contains a simplified summary of the complex theory, neglecting the spin dependence. The potential within the nucleus is unknown; hence, it is not possible to directly calculate the inner region wave function of the angular momentum l . Instead, the linear combination of the eigenfunctions corresponding to the energy states in the compound nucleus is used to represent wave function $\phi_l(E, r)$, as shown in Eq. (1).

$$\phi_l(E, r) = \sum_{\lambda} A_{l\lambda} \phi_l(E_{\lambda}, r) , \quad (1)$$

where A_{λ} is the normalization factor.

The wave function and eigenfunctions are the solutions of the internal region Schrodinger equation in the radial direction as given in Eq. (2).

$$\begin{aligned} \left(\frac{d^2 \phi_l(E, r)}{dr^2} \right) + \frac{2M}{\hbar^2} \left(E - V(r) - \frac{l(l+1)}{2Mr^2} \hbar^2 \right) \phi_l(E, r) &= 0 \\ \left(\frac{d^2 \phi_l(E_{\lambda}, r)}{dr^2} \right) + \frac{2M}{\hbar^2} \left(E_{\lambda} - V(r) - \frac{l(l+1)}{2Mr^2} \hbar^2 \right) \phi_l(E_{\lambda}, r) &= 0 \end{aligned} \quad (2)$$

In the case of the boundary conditions, both functions vanish at $r=0$, and the logarithmic derivatives of the eigenfunctions are constant at the boundary surface $r=a$; where a is the interaction radius (channel radius).

$$\frac{(r\phi_l'(E_\lambda, r))_{r=a}}{\phi_l(E_\lambda, r)} = B_l \quad . \quad (3)$$

The normalization factor $A_{l\lambda}$ given in Eq. (1) is calculated using the orthogonality condition and the assumption that the eigenfunctions are normalized.

$$A_{l\lambda} = \int_0^a \phi_l(E, r)\phi_l(E_\lambda, r) dr \quad . \quad (4)$$

The simple mathematical manipulations of Eq. (2), such as multiplication, subtraction and integration over the inner region result in Eq. (5) below. Using the Eqs. (4) and (5), it is possible to express the normalization factor as shown in Eq. (6).

$$\{\phi_l(E_\lambda, a)\phi_l'(E, a) - \phi_l(E, a)\phi_l'(E_\lambda, a)\} + \frac{2M}{\hbar^2}(E - E_\lambda) \int_0^a \phi_l(E, r)\phi_l'(E_\lambda, r) dr = 0 \quad , \quad (5)$$

$$A_{l\lambda} = \frac{\hbar^2}{2M(E_\lambda - E)} \{\phi_l(E_\lambda, a)\phi_l'(E, a) - \phi_l(E, a)\phi_l'(E_\lambda, a)\} \quad . \quad (6)$$

Finally, by inserting the normalization factor expression into Eq. (1) and applying the boundary condition given in Eq. (3), the inner region wave function transforms into the following expression. The R-matrix is defined in Eq. (8).

$$\phi_l(E, r) = \left\{ \frac{\hbar^2}{2Ma} \sum_\lambda \frac{\phi_l(E_\lambda, a)\phi_l(E_\lambda, a)}{(E_\lambda - E)} \right\} [a\phi_l'(E_\lambda, a) - \phi_l(E, a)B_l] \quad , \quad (7)$$

$$R_l = \sum_\lambda \frac{\gamma_{l\lambda}\gamma_{l\lambda}}{(E_\lambda - E)} \quad , \quad (8)$$

where $\gamma_{l\lambda}$ is the reduced width amplitude given below.

$$\gamma_{l\lambda} = \sqrt{\frac{\hbar^2}{2Ma}} \phi_l(E_\lambda, a) \quad , \quad (9)$$

The energy level E_λ and reduced width amplitude $\gamma_{\lambda l}$ are evaluated by fitting the measured cross sections. The general form of the R-matrix is obtained by introducing the channels shown in Eq. (10), which include the possible pair of nucleon-nucleus and the corresponding spin of the pairs.

$$R_{cc'} = \sum_{\lambda} \frac{\gamma_{\lambda c} \gamma_{\lambda c'}}{(E_{\lambda} - E)} , \quad (10)$$

where c is the incident channel; c' is the exit channel; and the reduced width amplitude corresponding to the level λ and channel c is given below.

$$\gamma_{\lambda c} = \sqrt{\frac{\hbar^2}{2M_c a_c}} \phi_l(E_{\lambda}, a_c) . \quad (11)$$

The resonance microscopic partial and total cross sections are calculated using the collision matrix elements $U_{cc'}$ as shown in Eq. (12) and (13), respectively.

$$\sigma_{cc'} = \frac{\pi}{k^2} g_c |\delta_{cc'} - U_{cc'}|^2 , \quad (12)$$

$$\sigma_t = \sum_{c'} \sigma_{cc'} = \frac{2\pi}{k^2} g_c (1 - \text{Re}\{U_{cc'}\}) , \quad (13)$$

where the collision matrix is symmetric and unitary; k is the wave number; and g_c is the statistical factor, the function of compound nucleus spin J , and target nucleus spin I . The collision matrix element $U_{cc'}$ is defined in terms of the matrix R and level matrix A , as shown in Eq. (14) below.

$$\begin{aligned} U_{cc'} &= e^{-i(\phi_c + \phi_{c'})} \left\{ \delta_{cc'} + iP_c^{1/2} \left[(1 - RL^0) R \right]_{cc'} P_{c'}^{1/2} \right\} \\ &= e^{-i(\phi_c + \phi_{c'})} \left\{ \delta_{cc'} + i \sum_{\lambda, \mu} \Gamma_{\lambda c}^{-1/2} A_{\lambda \mu}^{-1} \Gamma_{\mu c'}^{-1/2} \right\} , \end{aligned} \quad (14)$$

$$A_{\lambda \mu} = (E_{\lambda} - E) \delta_{\lambda \mu} - \sum_c \gamma_{\lambda c} L_{cc}^0 \gamma_{\mu c} , \quad (15)$$

$$L_{cc}^0 = (S_c - B_c + iP_c) , \quad (16)$$

where $\Gamma_{\lambda x} = (2P_x)^{1/2} \gamma_{\lambda x}$ is the channel x width (given in nuclear data files); L^0 is the diagonal matrix; S_c and P_c are shift and penetration factors, respectively; ϕ_c is the hard-sphere shift factor; and B_c is the arbitrary boundary parameter.

Depending on assumptions made, there are conventional formalisms applied to reconstruct the resonance microscopic cross sections [4, 9]. Currently, single-level Breit-Wigner (SLBW), multilevel Breit-Wigner (MLBW), Reich-Moore (RM), and R-matrix Limited (RML) formalisms are in practical use. **Table 1** provides a short summary of the ENDF/B-VII.1 neutron-induced library. In the given nuclear data, 331 isotopes contain the resonance parameters used to generate the resolved resonance cross sections and the remaining 92 isotope – only point-wise cross section in File 3. More detailed information on the formalisms are provided in Chapter III.

Table 1. Summary on ENDF/B-VII.1 isotopes.

RESONANCE PARAMETERS	METHOD	NUMBER OF ISOTOPES
YES	SLBW	8
	MLBW	268
	RM	54
	RML	1
NO	point-wise XS	92
	Total	423

It is important to note that cross sections reconstructed using formalisms based on R-matrix theory are at 0 K temperature; in other words, the target nucleus is at rest in the laboratory system. According to the nuclear reactor type there is need in the wide range of temperature dependent cross sections data.

2.2 Multipole Representation

The multipole representation was first proposed by Hwang [4-7] as an alternative to the conventional formalisms SLBW, MLBW, and RM. The collision matrix must be single valued and meromorphic in momentum space, which allows us to represent a cross section as the sum of the Lorentzian terms. Eqs. (17), (18), and (19) demonstrate the rigorous multipole formulae to obtain capture/fission, total, and elastic scattering cross sections, respectively.

$$\sigma_{x=\gamma,f}(E) = \frac{1}{E} \sum_{l,J} \sum_{\lambda}^N \sum_{j=1}^{2(l+1)} \operatorname{Re} \left[\frac{(-iR_{l,J,\lambda,j}^{(x)})}{p_{l,J,\lambda,j}^* - \sqrt{E}} \right], \quad (17)$$

$$\sigma_t(E) = \sigma_i(E) + \frac{1}{E} \sum_{l,J} \sum_{\lambda}^N \sum_{j=1}^{2(l+1)} \operatorname{Re} \left[\frac{(-ie^{-i2\phi_l} R_{l,J,\lambda,j}^{(t)})}{p_{l,J,\lambda,j}^* - \sqrt{E}} \right], \quad (18)$$

$$\sigma_s = \sigma_t - \sigma_f - \sigma_\gamma, \quad (19)$$

where λ , N are the resonance index and the total number of resonances; $R_{l,J,\lambda,j}^{(x)}$, $p_{l,J,\lambda,j}^*$, E are the residue corresponding to the reaction x , the complex conjugate of the resonance pole, and energy, respectively.

The main advantage of the given approach over the methods widely used to generate cross sections is the capability to apply analytical Doppler broadening. In other words, the resonance microscopic cross sections at any temperature of the interest are directly reconstructed from multipole parameters as shown in Eqs. (20) and (21).

$$\sigma_{x=\gamma,f}(E) = \frac{1}{E} \sum_{l,J} \sum_{\lambda}^N \sum_{j=1}^{2(l+1)} \frac{\operatorname{Re} \left[R_{l,J,\lambda,j}^{(x)} \sqrt{\pi} W(z_0) - \frac{-iR_{l,J,\lambda,j}^{(x)}}{\sqrt{\pi}} C \left(\frac{p_{l,J,\lambda,j}^*}{\sqrt{\xi}}, \frac{\sqrt{E}}{2\sqrt{\xi}} \right) \right]}{2\sqrt{\xi}}, \quad (20)$$

$$\sigma_t(E) = \sigma_p(E) + \frac{1}{E} \sum_{l,J} \sum_{\lambda}^N \sum_{j=1}^{2(l+1)} \frac{\operatorname{Re} \left[R_{l,J,\lambda,j}^{(t)} \sqrt{\pi} W(z_0) - \frac{-iR_{l,J,\lambda,j}^{(t)}}{\sqrt{\pi}} C \left(\frac{p_{l,J,\lambda,j}^*}{\sqrt{\xi}}, \frac{\sqrt{E}}{2\sqrt{\xi}} \right) \right]}{2\sqrt{\xi}}, \quad (21)$$

$$C \left(\frac{z}{\sqrt{\xi}}, \frac{u}{2\sqrt{\xi}} \right) = 2z \int_0^\infty \frac{du'}{z^2 - u'^2} \times \exp \left(-\frac{u+u'}{4\xi} \right)^2, \quad (22)$$

where $z_0 = \frac{\sqrt{E} - p_{l,J,\lambda,j}^*}{2\sqrt{\xi}}$; $\xi = \frac{k_b T}{4A}$; T is target temperature; z is the complex variable; $W(z)$ is

the complex probability integral (Faddeeva function); and $u = \sqrt{E}$. Eq. (22) provides the expression for the correction term used to properly Doppler broaden microscopic cross sections in the low energy region [4-7Error! Reference source not found.]. In general, the given term is negligible when EMBED Equation.DSMT4 $E \geq 1eV$ for most of the isotopes, since it exponentially vanishes. The

details on the Doppler broadening using Faddeeva function and its evaluation are described in Section 2.3.

However, the major difficulty caused by the given approach is obtaining multipole parameters; in other words, poles and residues. Chapter III provides details on converting processes from conventional formalisms formatted resonance parameters into rigorous multipoles.

2.3 Doppler broadening

In order to take into account, the thermal motion of the nucleus at the temperature of the interest during the neutron-nucleus interaction, microscopic cross sections need to be modified or Doppler broadened. The well-known Doppler-broadening equation is given below for target temperature T and reference temperature T_0 . The solution of Eq. (23) provides the microscopic cross section of the nuclei at the temperature of the interest T . The direct method to solve the Doppler-broadening equation is to use a tabulated cross section as done by SIGMA1 [10].

$$V\sigma(V,T) = \frac{1}{V} \left(\frac{\beta}{\pi} \right)^{1/2} \int_0^\infty [V_r \sigma(V_r, T_0)] V_r dV_r \times \left\{ e^{-\beta(V-V_r)^2} - e^{-\beta(V+V_r)^2} \right\}, \quad (23)$$

$$\beta = \frac{m}{2k_b(T-T_0)}, \quad (24)$$

where V is speed of neutrons; V_r is relative speed between the monoenergetic neutron beam and the target nuclei; T_0 is the temperature below target temperature T ; k_b is the Boltzmann constant; and m is the mass of the projectile (neutron).

Another well-known Doppler broadening technique is analytical broadening using Doppler-broadened Line-Shape functions. To use the given method, the cross sections need to be expanded in pole and residue form (Lorentzian-like terms), as shown in Section 2.2. Application of the Doppler-broadened line-shape functions to reconstruct temperature dependent cross sections is possible for conventional SLBW and MLBW formalisms [9].

$$W(z) = \frac{i}{\pi} \int_{-\infty}^{\infty} \frac{e^{-t^2} dt}{z-t}, \quad (25)$$

$$\sqrt{\pi} y W(z) = \psi(x, y) + i\chi(x, y), \quad (26)$$

where $z = x + iy$ is the complex variable; and $\psi - \chi$ are Doppler-broadened line-shape functions.

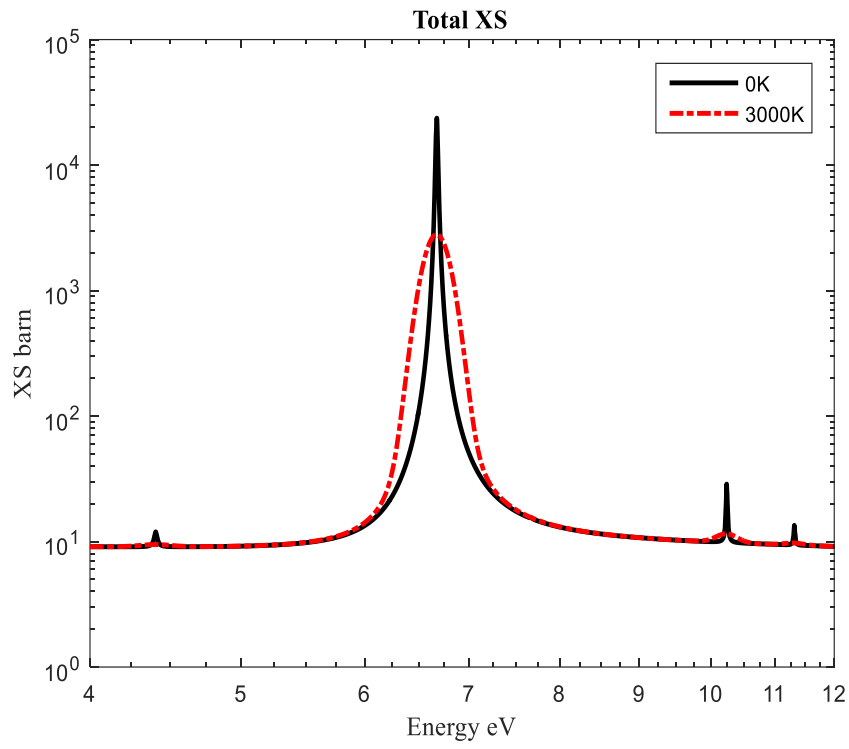


Figure 1. Resonance cross section comparison at 0 K and 3000 K temperatures.

III. Converting Resonance Parameters

This chapter describes the conversion of the resonance parameters given in the evaluated nuclear data files into multipole parameters. Single-level and multilevel Breit-Wigner format resonances are processed in Section 3.1. In the case of Reich-Moore formalism, the process and issues associated with it are provided in Section 3.2.

3.1 Breit-Wigner Formalisms

Breit-Wigner approximations require the application of a level matrix to represent resonance microscopic cross sections. There are two assumptions regarding the boundary constants as shown in Eq. (27) based on Breit-Wigner formalisms. By accepting the expressions in Eq. (27) and the substitution into Eq. (16), the level matrix element in Eq. (15) transforms into the expression given in Eq. (28) below.

$$B_n = S_l(E_\lambda) \quad \text{and} \quad B_{x=\gamma,f} = S_{x=\gamma,f} \quad , \quad (27)$$

$$A_{\lambda\mu} = \left[E_\lambda - \Delta_\lambda^{(l)}(u) - u^2 \right] \delta_{\lambda\mu} - \frac{i}{2} \sum_x \Gamma_{\lambda x}^{1/2} \Gamma_{\mu x}^{1/2} \quad , \quad (28)$$

where E_λ is the resonance energy; $\Gamma_{\lambda x}$ is the resonance width associated with channel $x = n, f, \gamma$; $\Gamma_{\lambda n}(u)$ is the energy dependent neutron width defined in Eq. (30); and $\Delta_\lambda^{(l)}(u)$ is the shift factor defined in Eq. (31). An example of constructing a level matrix is given in APPENDIX A. **Table 2** shows the important functions dependent on orbital angular momentum l , which are used to calculate level shift factor S_l and penetration factor P_l given in Eq. (29).

Table 2. Important orbital momentum dependent functions.

l	$q_l(u)$	$s_l(u)$	$\phi_l(u)$
0	1	0	ρ
1	$1 + \rho^2$	1	$\rho - \tan^{-1}[\rho]$
2	$9 + 3\rho^2 + \rho^4$	$18 + 3\rho^2$	$\rho - \tan^{-1}\left[\frac{\rho}{(3 - \rho^2)}\right]$
3	$225 + 45\rho^2 + 6\rho^4 + \rho^6$	$675 + 90\rho^2 + 6\rho^4$	$\rho - \tan^{-1}\left[\frac{\rho(15 - \rho^2)}{(15 - 6\rho^2)}\right]$

$$S_l(u) = \frac{s_l(u)}{q_l(u)} \quad \text{and} \quad P_l(u) = \frac{\rho^{2l+1}}{q_l(u)} \quad , \quad (29)$$

$$\Gamma_{\lambda n}^{(l)}(u) = \frac{P_l(u)}{P_l(|E_\lambda|)} \Gamma_{\lambda n} \quad , \quad (30)$$

$$\Delta_\lambda^{(l)}(u) = \frac{S_l(|E_\lambda|) - S_l(u)}{2P_l(|E_\lambda|)} \Gamma_{\lambda n} \quad , \quad (31)$$

where $\rho = \rho_0 u$; $\rho_0 = k_0 a$; a is the channel radius; $k_0 = 0.002196771 \times \frac{A}{A+1}$; and A is the isotopic mass.

Radiative capture and fission cross sections for both single-level and multilevel Breit-Wigner approximations have the same formulae - shown in Eq. (32) below. The major difference between those formalisms is the interference cross sections given in Eq. (36).

$$\sigma_{nx} = \sum_\lambda \sigma_{nx}^{(\lambda)} = \sum_\lambda \sum_{l,J} \frac{\pi}{k^2} g_J \left| \frac{\Gamma_{\lambda n}^{1/2}(u) \Gamma_{\lambda x}^{1/2}}{A_\lambda} \right|^2 \quad , \quad (32)$$

$$\sigma_i^{SLBW} = \sigma_p + \sum_\lambda \sigma_i^{(\lambda)} = \sigma_p + \sum_{l,J} \frac{2\pi}{k^2} g_J \operatorname{Re} \left\{ -ie^{-i2\phi} \frac{\Gamma_{\lambda n}^{1/2}(u) \Gamma_{\lambda n}^{1/2}(u)}{A_\lambda} \right\} \quad , \quad (33)$$

$$\sigma_p = \sum_\lambda \sum_{l,J} \frac{2\pi}{k^2} g_J \operatorname{Re} \{ 1 - e^{-i2\phi} \} \quad , \quad (34)$$

$$\sigma_i^{MLBW} = \sigma_i^{SLBW} + \sigma_{\text{int}} \quad , \quad (35)$$

$$\sigma_{\text{int}} = \sum_{l,J} \frac{\pi}{k^2} g_J \operatorname{Re} \left\{ \sum_\lambda \sum_{\mu \neq \lambda} \frac{\Gamma_{\lambda n}^{(l)}(u) \Gamma_{\mu n}^{(l)}(u)}{A_\lambda(u) A_\mu^*(u)} \right\} \quad . \quad (36)$$

In order to calculate poles corresponding to the resonance λ , polynomial of order $2(l+1)$ in Eq. (37) need to be solved. By substituting the level matrix element given in Eq. (28) and function q_l defined in **Table 2**, the coefficients are derived in terms of the resonance parameters from nuclear data files. The complex coefficients depending on the momentum l are given from Eq. (38) to Eq. (41).

$$q_l(u) A_\lambda(u) = \sum_{k=0}^{2(l+1)} a_k u^k = 0 \quad , \quad (37)$$

$$l=0 \rightarrow \begin{cases} a_0 = -\frac{i\Gamma_{\lambda f}}{2} - \frac{i\Gamma_{\lambda \gamma}}{2} + E_\lambda \\ a_1 = -\frac{i\Gamma_{\lambda n}}{2\sqrt{E_\lambda}} \\ a_2 = -1 \end{cases}, \quad (38)$$

$$l=1 \rightarrow \begin{cases} a_0 = E_\lambda - \frac{i}{2}(\Gamma_{\lambda f} + \Gamma_{\lambda \gamma}) + \frac{\Gamma_{\lambda n}}{2\sqrt{E_\lambda}\rho_0} \\ a_1 = 0 \\ a_2 = \rho_0^2 \left[E_\lambda - \frac{i}{2}(\Gamma_{\lambda f} + \Gamma_{\lambda \gamma}) \right] - 1 - \frac{\Gamma_{\lambda n}}{2E_\lambda^{3/2}\rho_0} \\ a_3 = -\frac{i\Gamma_{\lambda n}}{2E_\lambda^{3/2}} - \frac{i\Gamma_{\lambda n}\rho_0^2}{2\sqrt{E_\lambda}} \\ a_4 = -\rho_0^2 \end{cases}, \quad (39)$$

$$l=2 \rightarrow \begin{cases} a_0 = 9 \left[E_\lambda - \frac{i}{2}(\Gamma_{\lambda \gamma} + \Gamma_{\lambda f}) \right] + \frac{27\Gamma_{\lambda n}}{2E_\lambda^{3/2}\rho_0^3} + \frac{9\Gamma_{\lambda n}}{\sqrt{E_\lambda}\rho_0} \\ a_1 = 0 \\ a_2 = 3\rho_0^2 \left[E_\lambda - \frac{i}{2}(\Gamma_{\lambda \gamma} + \Gamma_{\lambda f}) \right] - 9 - \frac{27\Gamma_{\lambda n}}{2E_\lambda^{5/2}\rho_0^3} + \frac{3\Gamma_{\lambda n}\rho_0}{2\sqrt{E_\lambda}} \\ a_3 = 0 \\ a_4 = \rho_0^4 \left[E_\lambda - \frac{i}{2}(\Gamma_{\lambda \gamma} + \Gamma_{\lambda f}) \right] - \frac{9\Gamma_{\lambda n}}{E_\lambda^{5/2}\rho_0} - \frac{3\Gamma_{\lambda n}\rho_0}{2E_\lambda^{3/2}} - 3\rho_0^2 \\ a_5 = -\frac{9i\Gamma_{\lambda n}}{2E_\lambda^{5/2}} - \frac{3i\Gamma_{\lambda n}\rho_0^2}{2E_\lambda^{3/2}} - \frac{i\Gamma_{\lambda n}\rho_0^4}{2\sqrt{E_\lambda}} \\ a_6 = -\rho_0^4 \end{cases}, \quad (40)$$

$$l=3 \rightarrow \left\{ \begin{array}{l}
 a_0 = 225 \left[E_\lambda - \frac{i}{2} (\Gamma_{\lambda\gamma} + \Gamma_{\lambda f}) \right] + \frac{10125\Gamma_{\lambda n}}{2E_\lambda^{5/2}\rho_0^5} + \frac{1350\Gamma_{\lambda n}}{E_\lambda^{3/2}\rho_0^3} + \frac{675\Gamma_{\lambda n}}{2\sqrt{E_\lambda}\rho_0} \\
 a_1 = 0 \\
 a_2 = 45\rho_0^2 \left[E_\lambda - \frac{i}{2} (\Gamma_{\lambda\gamma} + \Gamma_{\lambda f}) \right] - 225 - \frac{10125\Gamma_{\lambda n}}{2E_\lambda^{7/2}\rho_0^5} + \frac{135\Gamma_{\lambda n}}{E_\lambda^{3/2}\rho_0} + \frac{45\Gamma_{\lambda n}\rho_0}{\sqrt{E_\lambda}} \\
 a_3 = 0 \\
 a_4 = -\frac{1350\Gamma_{\lambda n}}{E_\lambda^{7/2}\rho_0^3} - \frac{135\Gamma_{\lambda n}}{E_\lambda^{5/2}\rho_0} - 45\rho_0^2 + \frac{3\Gamma_{\lambda n}\rho_0^3}{\sqrt{E_\lambda}} - 3i\Gamma_{\lambda f}\rho_0^4 - 3i\Gamma_{\lambda\gamma}\rho_0^4 + 6E_\lambda\rho_0^4 \quad . \quad (41) \\
 a_5 = 0 \\
 a_6 = \rho_0^6 \left[E_\lambda - \frac{i}{2} (\Gamma_{\lambda\gamma} + \Gamma_{\lambda f}) \right] - \frac{675\Gamma_{\lambda n}}{2E_\lambda^{7/2}\rho_0} - \frac{45\Gamma_{\lambda n}\rho_0}{E_\lambda^{5/2}} - \frac{3\Gamma_{\lambda n}\rho_0^3}{E_\lambda^{3/2}} - 6\rho_0^4 \\
 a_7 = -\frac{225i\Gamma_{\lambda n}}{2E_\lambda^{7/2}} - \frac{45i\Gamma_{\lambda n}\rho_0^2}{2E_\lambda^{5/2}} - \frac{3i\Gamma_{\lambda n}\rho_0^4}{E_\lambda^{3/2}} - \frac{i\Gamma_{\lambda n}\rho_0^6}{2\sqrt{E_\lambda}} \\
 a_8 = -\rho_0^6
 \end{array} \right.$$

As soon as the poles are calculated, the next step is to generate the residues associated with the total, absorption, fission cross sections, and the interference cross section in the case of MLBW formalism. The first residue to calculate is associated with the total reaction cross section using Eq. (42) below. The capture and fission residues are obtained using the already calculated total residue as shown in Eq. (43). Absorption residue is calculated by summation of capture and fission residues. The interference residue is generated using Eq. (44).

$$R_{l,J,\lambda,j}^{(t)} = \frac{2\pi}{k_0^2} g_J \times \frac{q_l(p_{l,J,\lambda,j}^*) \times \Gamma_{\lambda n}^{(l)}(p_{l,J,\lambda,j}^*)}{-\rho_0^{2l} \prod_{\substack{k=1 \\ k \neq j}}^{2(l+1)} (p_{l,J,\lambda,j}^* - p_{l,J,\lambda,k}^*)} \quad , \quad (42)$$

$$R_{l,J,\lambda,j}^{(x=\gamma,f)} = R_{l,J,\lambda,j}^{(t)} \times \frac{\Gamma_{\lambda n}}{\Gamma_{\lambda n}^{(l)}(p_{l,J,\lambda,j}^*) + \Gamma_{\lambda\gamma} + \Gamma_{\lambda f}} \quad , \quad (43)$$

$$R_{l,J,\lambda,j}^{(\text{int})} = R_{l,J,\lambda,j}^{(t)} \times i \left[\sum_{\mu \neq \lambda} \frac{\Gamma_{\mu n}^{(l)}(p_{l,J,\lambda,j}^*)}{[A_\mu(p_{l,J,\lambda,j}^*)]^*} \right] \quad . \quad (44)$$

As soon as the converting of the Breit-Wigner resonance parameters are converted into corresponding poles and residues, the cross section can be reconstructed. **Figure 2** demonstrates the

^{241}Am (MLBW) isotope total, elastic scattering, and absorption cross sections at 0 K temperature generated using poles and residues.

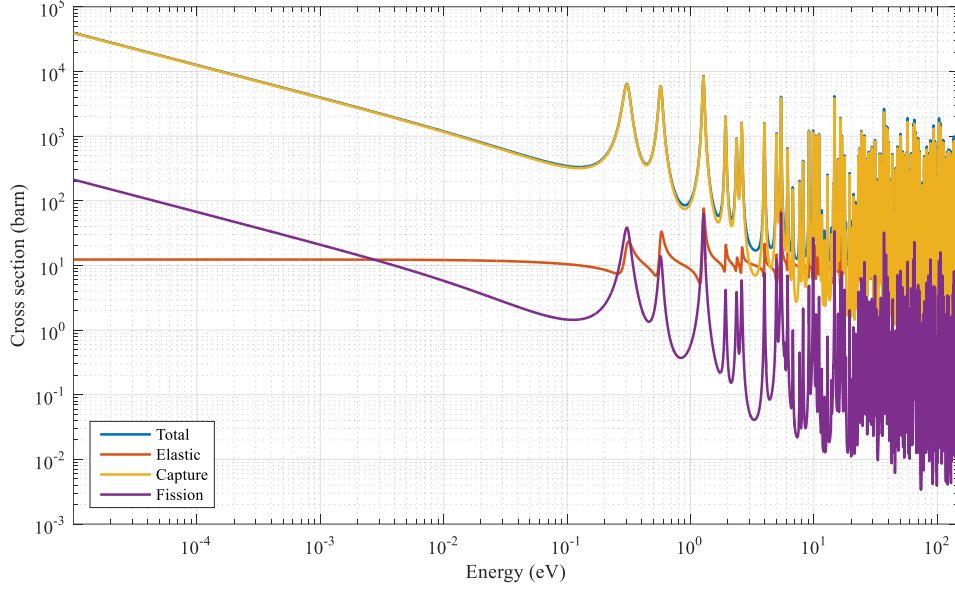


Figure 2. Multipole reconstructed cross sections of ^{241}Am at 0 K temperature.

3.2 Reich-Moore Formalism

The collision matrix is represented in terms of a channel matrix $(I - K)$ in Eq. (45). The expression of the channel matrix element is given in Eq. (46). In addition, APPENDIX A contains an example of constructing channel matrix using artificial resonance parameters.

$$U_{cc'} = e^{-i(\phi_c + \phi_{c'})} \left[2(I - K)_{cc'}^{-1} - \delta_{cc'} \right], \quad (45)$$

$$(I - K)_{cc'} = \delta_{cc'} - \frac{i}{2} \sum_{\lambda} \frac{\Gamma_{\lambda c}^{1/2} \Gamma_{\lambda c'}^{1/2}}{E_{\lambda} - u^2 - \frac{i}{2} \Gamma_{\lambda \gamma}}. \quad (46)$$

In order to convert the RM resonance parameters into the corresponding multipoles, the relation given in Eq. (47) between the channel matrix and the transmission probability is used. Substitution of the transmission probability into the collision matrix given in Eq. (45) results in the following expressions of the total, elastic scattering, absorption and fission reaction cross sections.

$$\rho_{cc'} = \delta_{cc'} - (I - K)_{cc'}^{-1}, \quad (47)$$

$$\sigma_t = \frac{2\pi}{k^2} \sum_{l,J} g_J \left[(1 - \cos 2\phi_l) + 2\text{Re}(e^{-2i\phi_l} \rho_{nm}) \right] , \quad (48)$$

$$\sigma_s = \sigma_t - \sigma_{abs} , \quad (49)$$

$$\sigma_{abs} = \sigma_t - \sigma_{nm}(E) = \frac{4\pi}{k^2} \sum_{l,J} g_J \left[\text{Re}(\rho_{nm}) - |\rho_{nm}|^2 \right] , \quad (50)$$

$$\sigma_{nf} = \frac{4\pi}{k^2} \sum_{l,J} g_J \left[|\rho_{nf1}|^2 + |\rho_{nf2}|^2 \right] . \quad (51)$$

The transmission probability elements can be represented as the ratio of polynomials of orders $(2M-1)$ in numerator and $(2M)$ in denominator [5], where $M = (l+1)N$ and N is the number of resonances. The sum of the Lorentzian terms can be used to represent the cross sections using Eqs. (52) and (53).

$$\rho_{nm} = \sum_{j=1}^{2M} \frac{r_{nj}}{p_j - u} , \quad (52)$$

$$|\rho_{nc}|^2 = \sum_{j=1}^{2M} \left[\frac{r_{cj}}{p_j - u} + \frac{r_{cj}^*}{p_j^* - u} \right] = \sum_{j=1}^{2M} \text{Re} \left\{ \frac{2r_{cj}}{p_j - u} \right\} . \quad (53)$$

The first step is to obtain the poles p_j using the Reich-Moore parameters from the nuclear data file. The polynomial $F(u)$ given in Eq. (54) of the very high order $2N(l+1)$ needs to be solved and the roots are the corresponding complex poles.

$$F(u) = \det(I - K) \times q_l(u) \times \prod_{\lambda}^N \left(E_{\lambda} - u^2 - \frac{i}{2} \Gamma_{\lambda\gamma} \right) = 0 . \quad (54)$$

The Newton Raphson method was implemented to calculate all the roots of the polynomial $F(u)$ one by one. Eq. (55) shows the iterative scheme and how the $(t+1)$ -th root is updated using the previous iteration root and the inverse of the logarithmic derivative of $F(u)$ at t -th iteration.

$$u^{t+1} = u^t - \frac{F(u)}{F'(u)} \Big|_{u^t} . \quad (55)$$

There are two main tasks to complete: (1) calculate the initial guesses for the iterative scheme, and (2) properly calculate the logarithmic derivative of the polynomial $F(u)$. Hwang suggested using the simplified polynomial given in Eq. (56) which consists of only single resonance information [5]. Eq. (57) shows the expression for the channel matrix consists of single resonance only. The complex coefficients are derived in the similar manner as was done in Section 3.1.

$$P_\lambda(u) = \det(I - K)_\lambda \times q_l(u) \times \left(E_\lambda - u^2 - \frac{i}{2} \Gamma_{\lambda\gamma} \right) = 0, \quad (56)$$

$$\left[(I - K)_{cc'} \right]_\lambda = \delta_{cc'} - \frac{i}{2} \frac{\Gamma_{\lambda c}^{1/2} \Gamma_{\lambda c'}^{1/2}}{E_\lambda - u^2 - \frac{i}{2} \Gamma_{\lambda\gamma}}, \quad (57)$$

$$l=0 \rightarrow \begin{cases} a_0 = -\frac{i\Gamma_{\lambda f}}{2} - \frac{i\Gamma_{\lambda\gamma}}{2} + E_\lambda \\ a_1 = -\frac{i\Gamma_{\lambda n}}{2\sqrt{E_\lambda}} \\ a_2 = -1 \end{cases}, \quad (58)$$

$$l=1 \rightarrow \begin{cases} a_0 = E_\lambda - \frac{i}{2} (\Gamma_{\lambda f} + \Gamma_{\lambda\gamma}) \\ a_1 = 0 \\ a_2 = \rho_0^2 \left[E_\lambda + -\frac{i}{2} (\Gamma_{\lambda f} + \Gamma_{\lambda\gamma}) \right] - 1, \\ a_3 = -\frac{i\Gamma_{\lambda n}}{2E_\lambda^{3/2}} - \frac{i\Gamma_{\lambda n}\rho_0^2}{2\sqrt{E_\lambda}} \\ a_4 = -\rho_0^2 \end{cases}, \quad (59)$$

$$l=2 \rightarrow \begin{cases} a_0 = 9 \left[E_\lambda - \frac{i}{2} (\Gamma_{\lambda\gamma} + \Gamma_{\lambda f}) \right] \\ a_1 = 0 \\ a_2 = 3\rho_0^2 \left[E_\lambda - \frac{i}{2} (\Gamma_{\lambda\gamma} + \Gamma_{\lambda f}) \right] - 9 \\ a_3 = 0 \\ a_4 = \rho_0^4 \left[E_\lambda - \frac{i}{2} (\Gamma_{\lambda\gamma} + \Gamma_{\lambda f}) \right] - 3\rho_0^2 \\ a_5 = -\frac{9i\Gamma_{\lambda n}}{2E_\lambda^{5/2}} - \frac{3i\Gamma_{\lambda n}\rho_0^2}{2E_\lambda^{3/2}} - \frac{i\Gamma_{\lambda n}\rho_0^4}{2\sqrt{E_\lambda}} \\ a_6 = -\rho_0^4 \end{cases}, \quad (60)$$

$$l=3 \rightarrow \begin{cases} a_0 = 225 \left[E_\lambda - \frac{i}{2} (\Gamma_{\lambda\gamma} + \Gamma_{\lambda f}) \right] \\ a_1 = 0 \\ a_2 = 45\rho_0^2 \left[E_\lambda - \frac{i}{2} (\Gamma_{\lambda\gamma} + \Gamma_{\lambda f}) \right] - 225 \\ a_3 = 0 \\ a_4 = -45\rho_0^2 - 3i\Gamma_{\lambda f}\rho_0^4 - 3i\Gamma_{\lambda\gamma}\rho_0^4 + 6E_\lambda\rho_0^4 \\ a_5 = 0 \\ a_6 = \rho_0^6 \left[E_\lambda - \frac{i}{2} (\Gamma_{\lambda\gamma} + \Gamma_{\lambda f}) \right] - 6\rho_0^4 \\ a_7 = -\frac{225i\Gamma_{\lambda n}}{2E_\lambda^{7/2}} - \frac{45i\Gamma_{\lambda n}\rho_0^2}{2E_\lambda^{5/2}} - \frac{3i\Gamma_{\lambda n}\rho_0^4}{E_\lambda^{3/2}} - \frac{i\Gamma_{\lambda n}\rho_0^6}{2\sqrt{E_\lambda}} \\ a_8 = -\rho_0^6 \end{cases}. \quad (61)$$

Another important step is to derive the logarithmic derivative of $F(u)$ used in the Newton Raphson iteration scheme. High order polynomial $F(u)$ consists of three main terms, which are shown in Eqs. (62), (63), and (64). By taking the logarithmic derivative of the polynomial, it is easy to derive the symbolic expression in terms of the momentum dependent functions as is given in Eq. (65).

$$f(u) = \prod_{\lambda}^N \left(E_\lambda - u^2 - \frac{i}{2} \Gamma_{\lambda\gamma} \right), \quad (62)$$

$$g(u) = q_l(u), \quad (63)$$

$$h(u) = \det(I - K) , \quad (64)$$

$$\frac{F'(u)}{F(u)} = \frac{f'(u)}{f(u)} + \frac{g'(u)}{g(u)} + \frac{h'(u)}{h(u)} . \quad (65)$$

Now, the logarithmic derivative of every term can be derived separately. Eqs. (66) and (67) show the logarithmic derivatives of the product term and the determinant of the channel matrix, respectively. **Table 3** provides the first order derivative of the orbital angular momentum l dependent function $q_l(u)$.

$$\frac{f'(u)}{f(u)} = \sum_{\lambda}^N \left(\frac{-2u}{E_{\lambda} - u^2 - \frac{i}{2}\Gamma_{\lambda\gamma}} \right) , \quad (66)$$

$$\frac{h'(u)}{h(u)} = -tr \left(\frac{adj(I - K)}{\det(I - K)} \frac{d(I - K)}{du} \right) = -tr \left((I - K)^{-1} \frac{dK}{du} \right) . \quad (67)$$

Table 3. The first order derivative of $q_l(u)$ function.

l	$q'_l(u)$
0	0
1	$2\rho_0^2 u$
2	$6\rho_0^2 u + 4\rho_0^4 u^3$
3	$90\rho_0 + 24\rho_0^3 + 6\rho_0^5$

Figure 3 demonstrates the pole distribution for ^{238}U , as well as the classifications. There are s-wavelike and not s-wavelike poles depending on the position on the complex plane. The former are concentrated along the real axis, while the latter are far from it, as shown in the figure below.

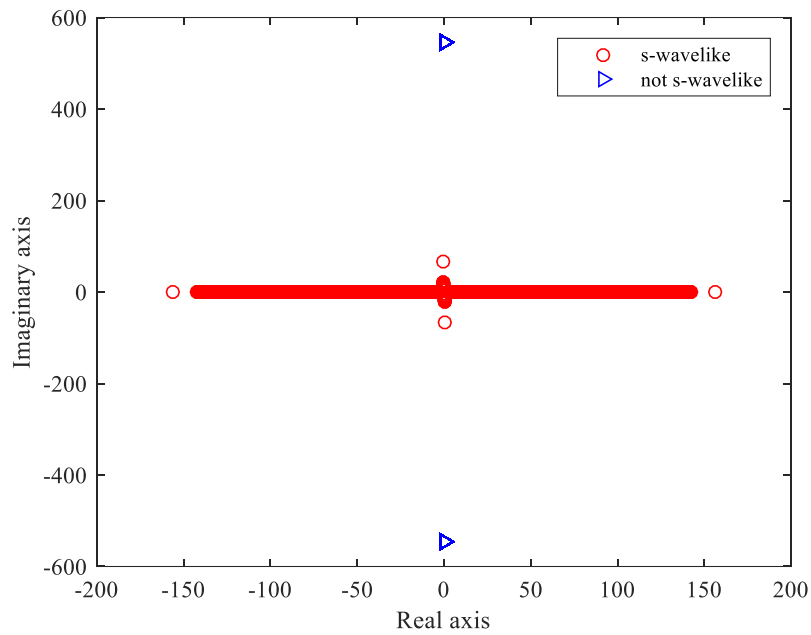


Figure 3. Distribution of poles for ^{238}U isotope.

The real and imaginary parts of the polynomial $F(u)$ constructed using the first 10 p-wave resonances of ^{238}U isotope are shown in **Figure 4** and **Figure 5**, respectively. As shown in figures below, s-wavelike poles are well separated and distinguishable from each other. Hence, those poles are easily obtained using the iterative approach.

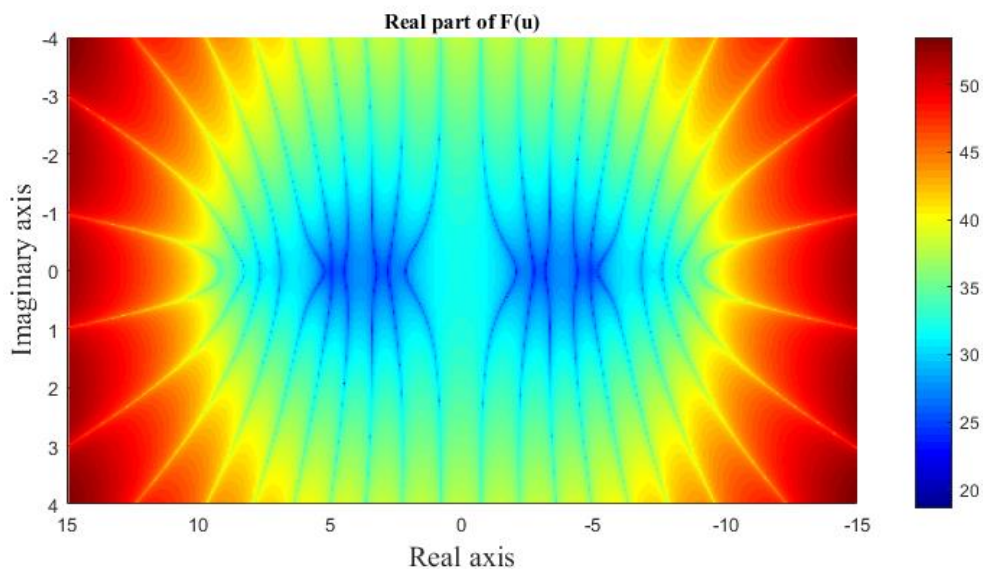


Figure 4. $\text{Re}(F(u))$: s-wavelike poles corresponding to the first 10 p-wave resonances of ^{238}U .

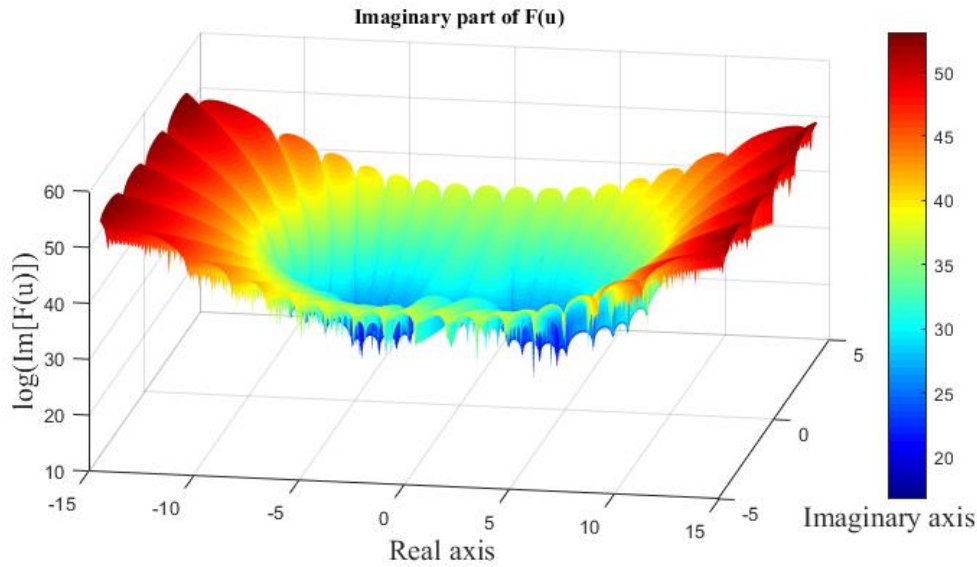


Figure 5. $\text{Im}(F(u))$: s-wavelike poles corresponding to the first 10 p-wave resonances of ^{238}U .

In general, every isotope contains $2N$ s-wavelike, and $2Nl$ not s-wavelike poles. The reason for the grouping is that the location of $2N$ poles for higher angular momentum resonances $l > 0$ is similar, as in the case of s-wave resonances. It is complicated to calculate all the complex roots of the high order polynomial $F(u)$ using the numerical methods. This problem is caused by the closely packed not s-wavelike poles, which are hardly distinguishable. **Figure 6** shows the highly packed initial guesses of not s-wavelike poles clusters positioned along the imaginary axis. True not s-wavelike clusters are slightly shifted along the imaginary axis.

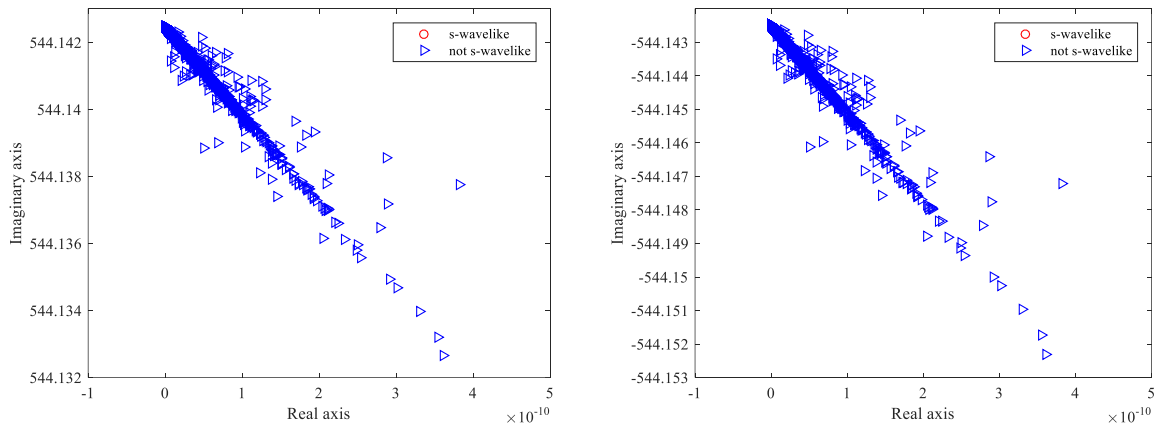


Figure 6. Not s-wavelike poles clusters along imaginary axis for ^{238}U isotope.

It is practically impossible to calculate every pole within the cluster. Instead of trials to obtain every separate not s-wavelike pole, approximations of the cluster using a single pole is preferable. In

other words, pseudo poles need to be calculated [5]. It was found that for p-wave resonances, $2N$ poles are located near to two zeros of Eq. (68). Any two initial guesses for not s-wavelike poles can be used as the basis for the calculation of pseudo poles via the Newton Raphson method.

$$1 + (\rho_0 u)^2 = 0 \quad . \quad (68)$$

As soon as the initial guesses for $2N$ s-wavelike and $2l$ pseudo poles are obtained, those values are used in the Newton Raphson iterative scheme to obtain the true poles corresponding to the Reich-Moore resonance parameters. The application of pseudo poles reduces the total number of multipole parameters from $2N(l+1)$ to $2(N+l)$.

Rigorous multipole representation allows us to directly reconstruct microscopic cross sections at various temperatures using the calculated poles and residues. **Figure 7** shows the ^{238}U isotope resolved resonance microscopic cross sections generated at 0 K.

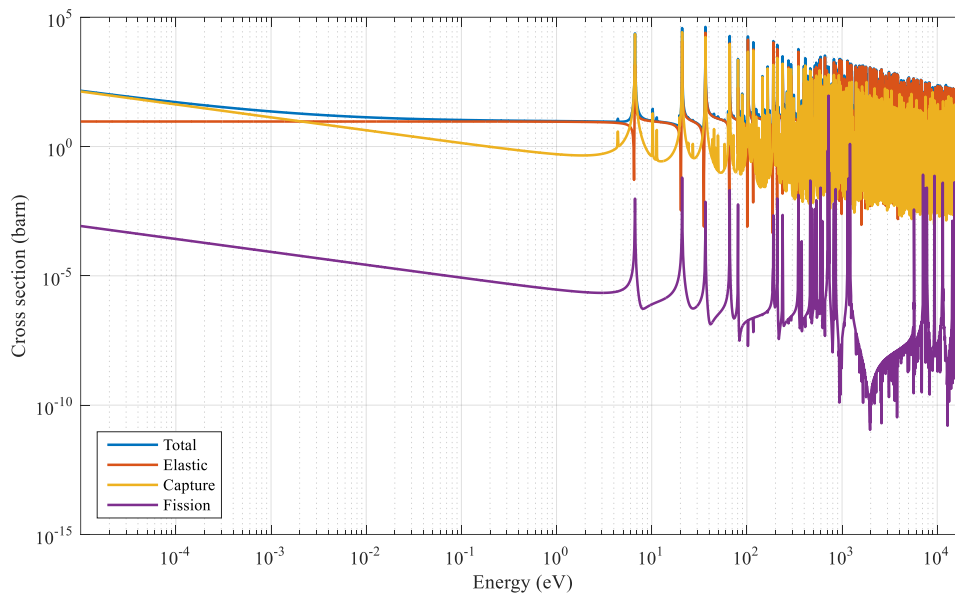


Figure 7. Multipole reconstructed cross sections of ^{238}U at 0 K temperature.

IV. Windowed Multipole Representation

A detailed description behind the windowed multipole representation [11-16] is given in this chapter. The window or energy window concept is summarized in Section 4.1. The polynomial fitting techniques used to reconstruct the background cross section are given in Section 4.2. In the final section of this chapter, the algorithm to generate the optimized windowed multipole library is provided.

4.1 Window Concept

Conventionally, the single energy point microscopic cross section is generated using all the resonance parameters given in the nuclear data file. In the case of rigorous multipole approach all the poles are used to reconstruct the cross section. This is the main disadvantage of the rigorous method, due to the large number of parameters as shown in Chapter III. To decrease XS generation time at a single energy point, the smooth behavior of the single resonance far from its peak is used. A similar trend was noticed in the case of multipole parameters. This is another important classification associated with the individual pole cross section behavior. Poles with positive real parts exhibit resonance behavior at the resonance energy, while the remaining counterparts have smooth contribution [11]. Hence, there are N fluctuating and remaining $N(2l+1)$ or $N+2l$ in the case of Breit-Wigner or Reich-Moore formalisms, respectively.

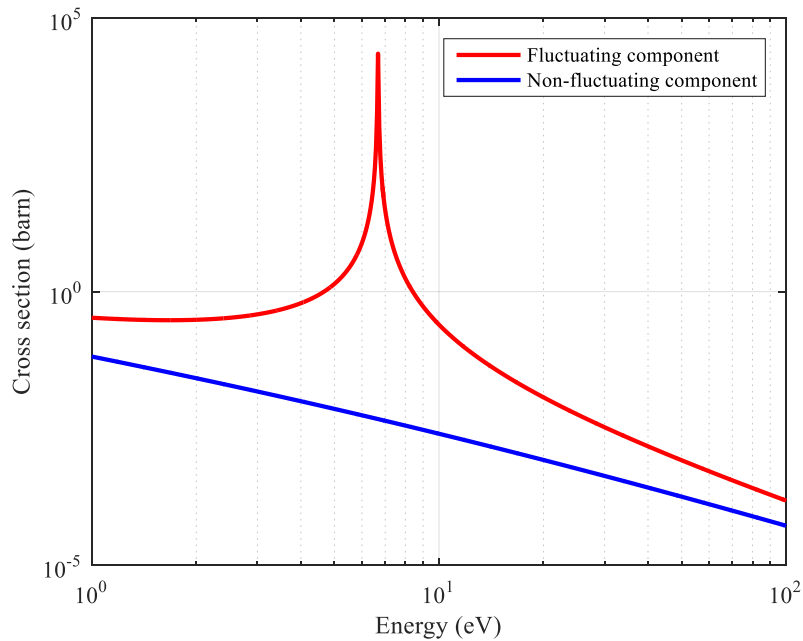


Figure 8. XS generated by poles corresponding to 6.673491 eV s-wave resonance of ^{238}U .

The peak and smooth contributions of fluctuating and non-fluctuation poles are presented in **Figure 8**. As shown in this figure, only fluctuating components create the resonance behavior of the microscopic cross section, and all the remaining components can be approximated using polynomial fitting. However, even though every single pole has a smooth contribution far from its resonance peak, the summation gives a very complicated background cross section. This cannot be fitted by a low order polynomial. In order to resolve the given issue, the energy window concept is used [12-15].

Basically, the resolved resonance energy range is divided into sub-intervals or inner windows uniformly. In order to reconstruct the cross section within one particular inner window, only the fluctuating poles within and nearby it's boundaries are required. The remaining poles give only smooth contributions which can be approximated by the polynomial. Hence, on top of every inner window there is an outer window, which contains all the important poles to reconstruct the resonance cross section. This approach enables us to decrease the number of poles used to reconstruct the cross section at every single energy point, and ignore all the non-fluctuating poles by applying low order polynomials. **Figure 9** shows the basic scheme of the window concept, with sub-intervals (inner windows) and corresponding outer windows. Cross sections constructed using the poles outside of the outer window are smooth and can be approximated.

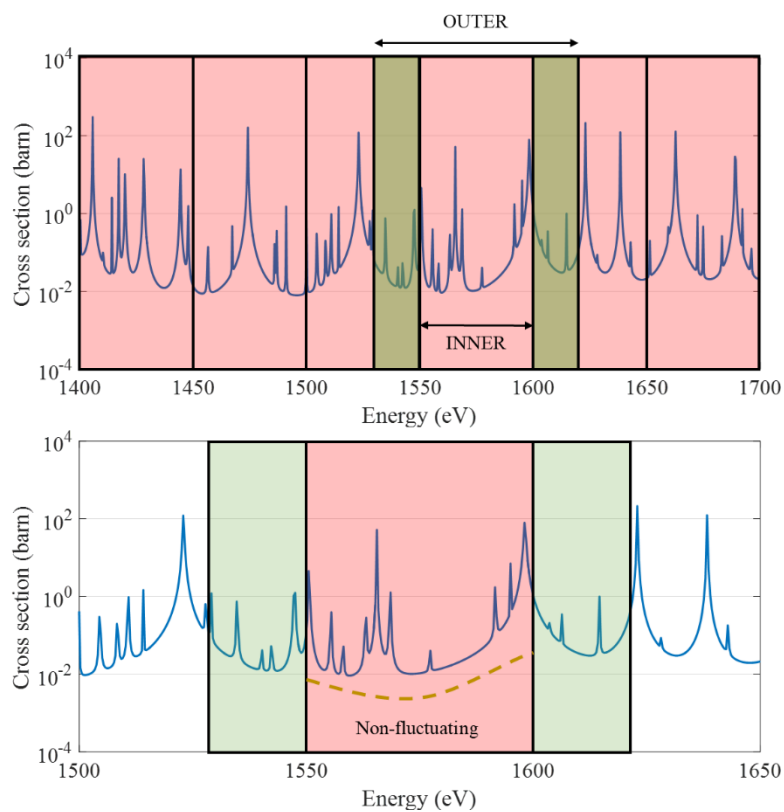


Figure 9. Window concept scheme (inner and outer windows).

The window concept allows us to minimize the number of evaluations of the Faddeeva function required for analytical Doppler broadening of the microscopic cross section at a single energy point. Section 4.2 contains a description on the polynomial fitting techniques used to compensate the background cross section from the omitted poles and File 3 of the evaluated nuclear data.

$$\sigma_i(E, T) = p(E) + \frac{1}{E} \sum_{l, J} \sum_{j \in \Omega_{outer}} \frac{\text{Re} \left[R_{l, J, \lambda, j}^{(l)} \sqrt{\pi} W(z_0(T)) \right]}{2\sqrt{\xi}}, \quad (69)$$

where E and T are the energy point and the temperature of interest; Ω_{outer} is the outer window index for the corresponding inner window; $p(E)$ is the fitting polynomial; the second term on the right hand side is summation over the poles j within the given outer window Ω_{outer} only.

4.2 Polynomial Fitting

The first technique is to perform polynomial fitting of the smooth cross section generated by the poles outside the outer window. According to the multipole representation, the cross section is expressed as the summation of the Lorentzian terms, which means that series expansion can be applied to each term in order to obtain the polynomial as shown in Eq. (70) below.

$$\sigma \propto \frac{1}{u^2} \left[\frac{r_j}{d_j - u} \right] \cong \frac{r_j}{d_j u^2} + \frac{r_j}{d_j^2 u} + \frac{r_j}{d_j^3} + \frac{r_j u}{d_j^4} + \frac{r_j u^2}{d_j^5} + O(u^3), \quad (70)$$

where $u < d_j$ must be satisfied.

Another polynomial fitting technique is required, when Eq. (70) is not valid due to the limitations and point-wise cross sections are provided by File 3 in the evaluated nuclear data. The least squares approach is used to compensate those background cross sections. Suppose that a cross section is approximated using polynomial $f(u)$ as shown in Eq. (71).

$$\sigma(u) \cong f(u) = a_{-2}(u)^{-2} + a_{-1}(u)^{-1} + a_0 + a_1(u) + a_2(u)^2 + \dots + a_M(u)^M, \quad (71)$$

where M is the polynomial order; and a_i is the expansion polynomial coefficients.

The given method of polynomial fitting minimizes the sum of squares of errors $S(a_1, a_2, a_3, \dots, a_M)$ in order to calculate the polynomial coefficients. The partial derivative of Eq. (72) with respect to each expansion coefficient is calculated as shown in Eq. (73). This allows us to obtain the linear system of M equations used to calculate the M expansion coefficients.

$$S(a_1, a_2, a_3, \dots, a_M) = \sum_{i=1}^N [f(u_i) - \sigma_i]^2, \quad (72)$$

$$\frac{\partial S}{\partial a_1} = \frac{\partial S}{\partial a_2} = \frac{\partial S}{\partial a_3} = \dots = \frac{\partial S}{\partial a_M} = 0, \quad (73)$$

where σ_i is the background cross section.

4.3 Windowed Multipole Library

There are several important parameters which need optimization in order to generate windowed multipole library for the specific isotope meeting the cross section error criteria. As explained in Section 4.1, inner and outer windows determine the number of poles used to reconstruct the temperature dependent cross section at single energy point. The order of the fitting polynomial highly depends on the number of poles within the outer window and the error criteria which need to be met. **Figure 10** shows the scheme to obtain the optimized inner and outer window sizes, and the polynomial order for any given isotope.

```

Convert Resonance Parameters into Multipoles
Initial guesses for inner window and outer window size

do inner window size:
  do outer window size:
    arrange poles indices ( $i_{low}, i_{up}$ ) for every inner window
    do inner window index:
      generate XS within the given window using ONLY poles ( $i_{low}, i_{up}$ )
      obtain background XS at 300 K and 3000 K
      do polynomial order = 2 : MAX(order)
        fitting of the background XS
        if error < 0.1 %
          break
      end do polynomial order
    end inner window index
  end do outer window
end do inner window size

```

Figure 10. Windowed multipole library generation algorithm.

The first step is to convert the resonance parameters from conventional formalisms into rigorous multipole parameters as described in Chapter III. As soon as poles and residues are obtained,

the windowed multipole library generation begins from initializing the inner and outer window sizes. As shown in **Figure 10**, for every inner window, fluctuating poles corresponding to the resonances within the outer window are assigned, or the first and the last pole indices are stored. Next, the cross section is generated within the inner window using the assigned poles and the background cross section corresponding to the neglected poles is obtained at different non-zero temperatures. Finally, attempts are made to fit the background cross sections using the polynomial of a different order until the cross section error criteria is met. In cases where no polynomial can be constructed, the outer window size is increased, and steps mentioned above are repeated. If even the change in the outer window size does not give the optimized parameters, the inner window size is decreased, and the entire process is repeated until the windowed multipole library is generated.

In the **APPENDIX B**, there is list of isotopes from ENDF/B-VII.1 neutron induced data bank which have been successfully converted into the windowed multipole library format, including the information on the resolved resonance upper energy limit, total number of poles, number of inner windows, order of polynomial fitting, and the time ratio between rigorous and windowed multipole reconstructed cross sections at single energy point at 0 K and 300 K temperatures. As can be observed from the time ratios, the window concept application has an obvious advantage over the rigorous multipole representation.

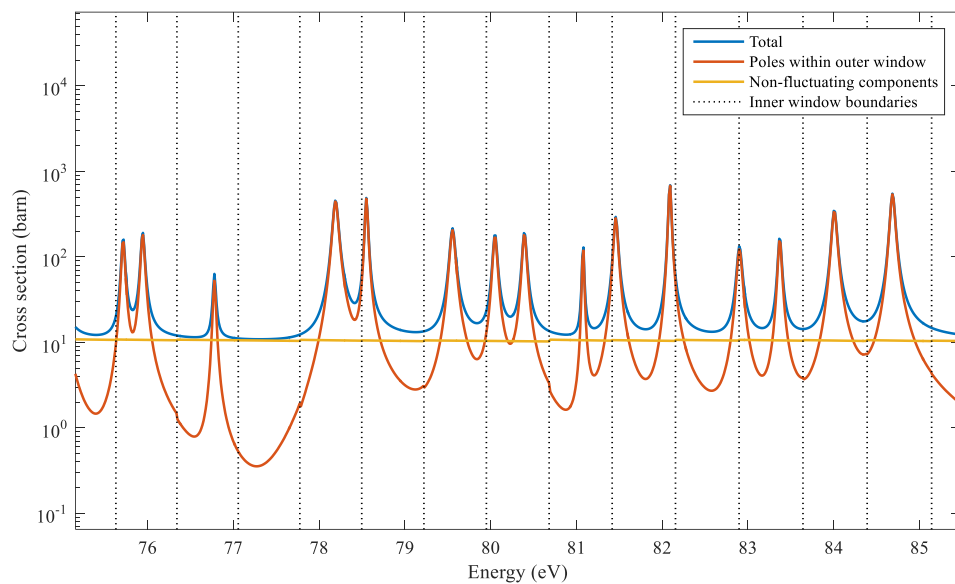


Figure 11. Window concept applied to ^{241}Am isotope.

The MLBW formatted resonance parameters of ^{241}Am undergo the converting process given in Section 3.1. This isotope contains only 194 s-wave resonances, which results in double the number

of poles. As already described, in the case of s-wave resonances, half of the poles are fluctuating and remaining are non-fluctuating. **Figure 11** illustrates the total cross section, cross section calculated using poles within outer windows, and non-fluctuating cross section fitted using low order polynomial for every inner window of ^{241}Am isotope.

V. Numerical Results

This chapter provides verification of the UNIST in-house generated windowed multipole library for 308 isotopes. Several single fuel pin-cell and fuel assembly problems were selected from the VERA benchmark suite [17]. Section 5.1 includes comparison results between on-the-fly Doppler broadening and a pre-generated ACE cross section treatment for single state, and the depletion calculation of selected fuel pins. Section 5.2 summarizes the application of the windowed multipole library in simulations of the chosen fuel assembly problems.

The VERA depletion benchmark suite provides a power density of 40W/gU and 40 step burnup points from 0 to 60MWD/kgU for the depletion calculation of neutron transport codes. **Table 4** shows 40 burnup points.

Table 4. The 40 step burnup points for depletion calculation.

Step	MWd/kgHM	Step	MWd/kgHM	Step	MWd/kgHM	Step	MWd/kgHM
1	0.00	11	7.00	21	17.00	31	37.50
2	0.01	12	8.00	22	18.00	32	40.00
3	0.25	13	9.00	23	19.00	33	42.50
4	0.50	14	10.00	24	20.00	34	45.00
5	1.00	15	11.00	25	22.50	35	47.50
6	2.00	16	12.00	26	25.00	36	50.00
7	3.00	17	13.00	27	27.50	37	52.50
8	4.00	18	14.00	28	30.00	38	55.00
9	5.00	19	15.00	29	32.50	39	57.50
10	6.00	20	16.00	30	35.00	40	60.00

5.1 PWR Fuel Pin

In the VERA benchmark specifications, there are ten single fuel pin-cell problems for four temperature and five enrichment configurations, and the presence of burnable poison material, which are widely used in LWRs. **Table 5** summarizes the VERA pin-cell problems, including not only UO₂ pin-cells, but also gadolinia (5% Gd₂O₃ + 95% UO₂, 1.8 wt.% ²³⁵U enriched) and IFBA pin problems. Among all the pin-cell problems 1C of the 3.1wt.% UO₂ fuel, and 1I of 5% gadolinia rods are selected. Pin-cell problem 1C is representative of normal fuel pin cases at the hot full power condition, and the problem 1I contains gadolinia which is the burnable poison material of the benchmark problem.

Table 5. VERA single pin depletion benchmark problems.

Problem	Description	Temperature (K)			²³⁵ U wt. %
		Moderator	Cladding	Fuel	
1A	Pin (3.1w/o)	565	565	565	3.1
1B	Pin (3.1w/o)	600	600	600	3.1
1C	Pin (3.1w/o)	600	600	900	3.1
1D	Pin (3.1w/o)	600	600	1200	3.1
1E	Pin (IFBA)	600	600	900	3.1
1F	Pin (2.1w/o)	600	600	900	2.1
1G	Pin (3.6w/o)	600	600	900	3.6
1H	Pin (4.6w/o)	600	600	900	4.6
1I	Pin (Gadolinia)	600	600	900	1.8
1J	Pin (3.1w/o)	600	600	600/900/1200	3.1

The UNIST in-house Monte Carlo code MCS depletion calculations of the chosen fuel pins are performed using ACE cross sections, and the on-the-fly Doppler broadening routine employing the pre-generated windowed multipole library. For the depletion calculation of pins 1C and 1I 100,000 histories are employed per cycle, 20 inactive and 200 active cycles.

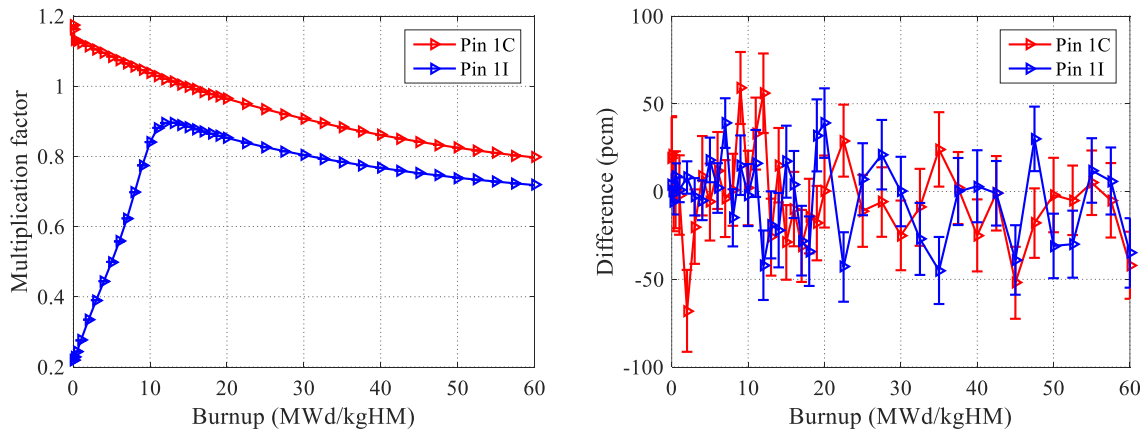


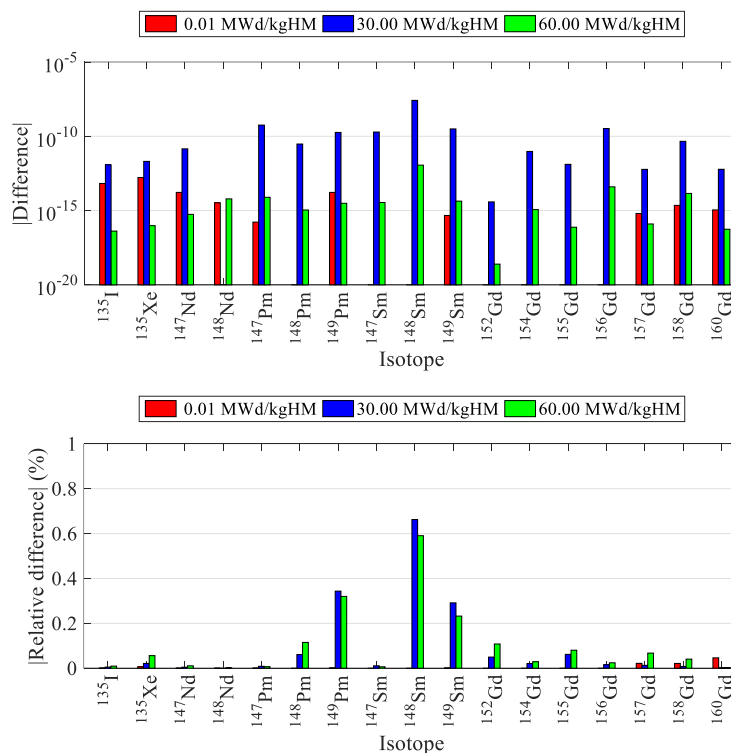
Figure 12. Multiplication factor comparison: ACE and WMP w.r.t. burnup for problems 1C, and 1I.

Figure 12 presents the multiplication factor comparison for problems 1C and 1I between ACE and windowed multipole library reconstructed cross sections. The k comparison shows good agreement between the reference ACE cross section data and the windowed multipole library throughout the depletion calculation.

Table 6. List of nuclides used for comparison study.

	Element	Isotope list
Fission Products	Iodine	135
	Xenon	135
	Neodymium	147, 148
	Promethium	147, 148, 149
	Samarium	147, 148, 149
Fission Products / Burnable Absorbers	Gadolinium	152, 154, 155, 156, 157, 158, 160
Important Actinides	Uranium	234, 235, 236, 237, 238
	Neptunium	237, 238, 239
	Plutonium	238, 239, 240, 241, 242, 243
	Americium	241, 242, 243
	Curium	242, 243, 244

In addition to the multiplication factor comparison, the isotope-wise number density difference is calculated at BOC, MOC, and EOC for pins 1C, and 1I. Important fission products, the burnable absorber, and actinides were selected to verify the windowed multipole library. The list of those nuclides is given in **Table 6**. The Pin 1C number density absolute difference and relative differences are illustrated in **Figure 13** and **Figure 14** for fission product and actinides, respectively. In the case of pin 1I, **Figure 15** and **Figure 16** show the comparison for the chosen isotopes.


Figure 13. Pin 1C absolute and relative differences in number density for fission products.

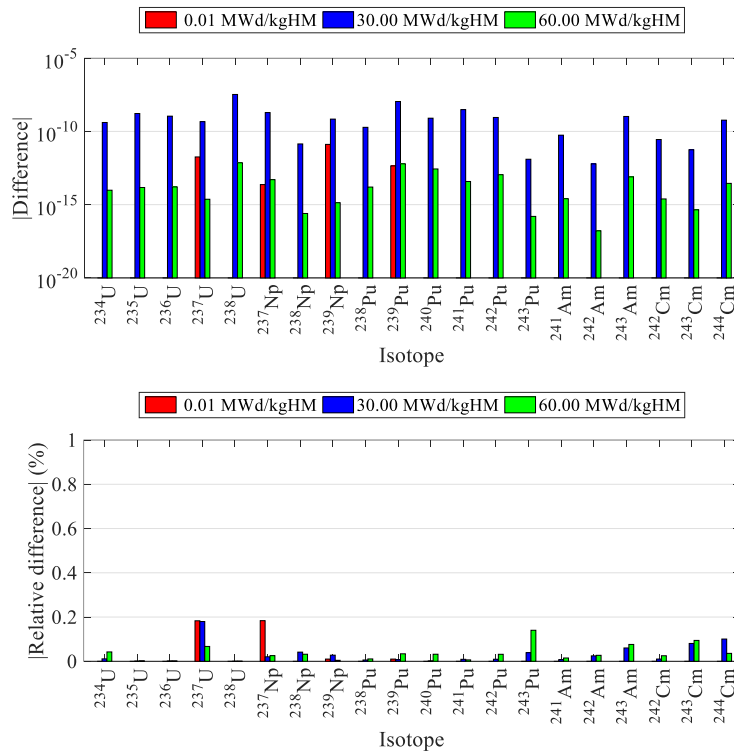


Figure 14. Pin 1C absolute and relative differences in number density for important actinides.

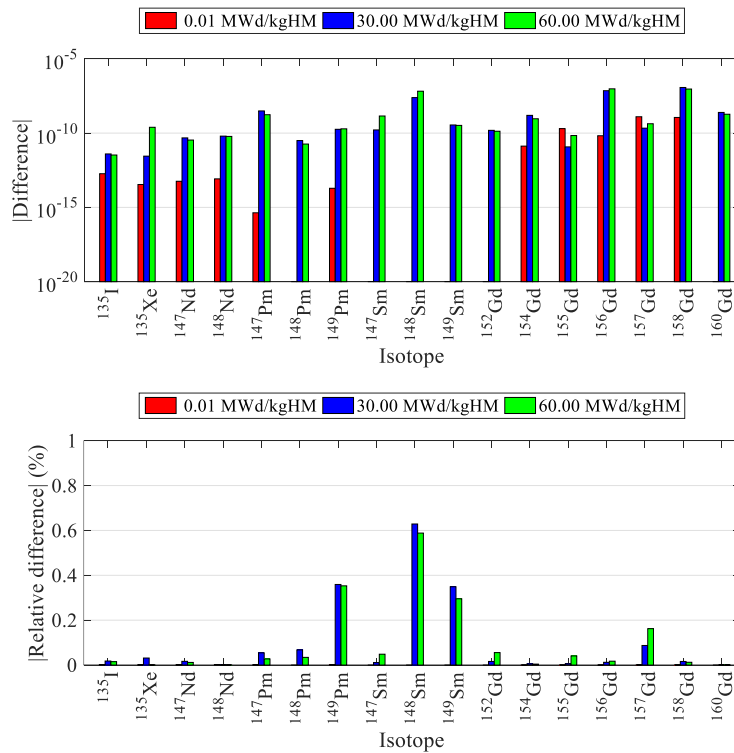


Figure 15. Pin 1I absolute and relative differences in number density for fission products.

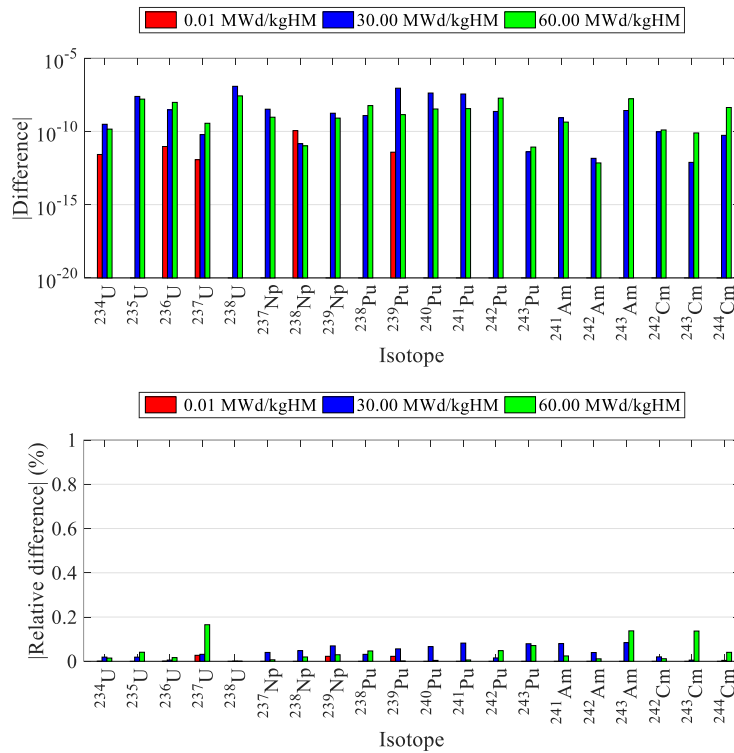


Figure 16. Pin 1I absolute and relative differences in number density for important actinides.

The absolute relative difference in the number density comparison between the ACE and WMP libraries used in the MCS depletion calculations is negligible according to the figures provided above. The relative difference is less than 0.7 % for fission products, and 0.2 % for important actinides; and the absolute difference is in the order of 10^{-8} for both 1C and 1I pin-cell problems

Next, the fresh and burned pins 1C and 1I are simulated at various temperatures starting from 0 K up to 1500 K. The isotope-wise reactivity error, absorption and fission reaction rates comparison between the ACE and WMP libraries are obtained for the given problems. It is important to note that all material temperatures, including fuel, air, cladding and coolant are the same and change from 0 K to 1500 K; in other words, there are 16 temperature points of comparison of the WMP library with reference ACE cross sections. The k_{inf} differences with corresponding standard deviations for pins 1C and 1I at 0.00 and 60.00 MWd/kgHM are illustrated in **Figure 17** at various temperatures. All the pin transport calculations are carried out using 100,000 particles per cycle for 50 inactive and 500 active cycles.

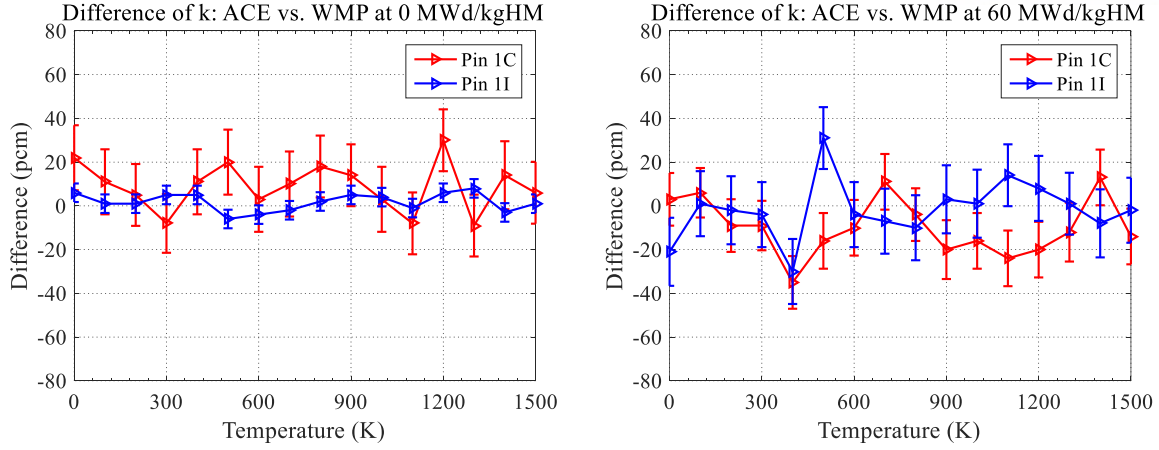


Figure 17. Difference of k : ACE and WMP w.r.t. temperature at 0.00 and 60.00 MWd/kgHM.

The isotope-wise reactivity error in group g and cell i is calculated using Eqs. (74) and (75) below [20]. The multiplication factor is calculated as the ratio of the volume integrated nu-fission reaction rate over the volume integrated absorption reaction rate.

$$\Delta\rho^{g,i,j} = \left(\frac{1}{k_{eff}^{ACE}} - \frac{1}{k_{eff}^{g,i,j}} \right) \times 10^5, \quad (74)$$

$$k_{eff}^{g,i,j} = \frac{\sum_{i'} \left[\left(\sum_{g'} \left(\sum_{j'} \nu R_{f,i',j'}^{ACE,g'} \right) \right) V_{i'} \right]}{\sum_{i'} \left[\left(\sum_{g'} \left(\sum_{j'} R_{a,i',j'}^{ACE,g'} \right) \right) V_{i'} \right] - R_{a,i,j}^{ACE,g} V_i + R_{a,i,j}^{WMP,g} V_i}, \quad (75)$$

where

$R_{a,i,j}^{ACE,g}$ = absorption reaction rate of isotope j (ACE) in group g and cell i ,

$R_{a,i,j}^{WMP,g}$ = absorption reaction rate of isotope j (WMP) in group g and cell i .

The calculated reactivity errors using the one group collision estimator reaction rate tallies with the corresponding standard deviations for fresh and burned 1C pin-cell problem, as shown in **Figure 18** and **Figure 19**. As clearly shown in the figures below, the isotope-wise reactivity errors are within three standard deviations for the chosen isotopes given in **Table 6**.

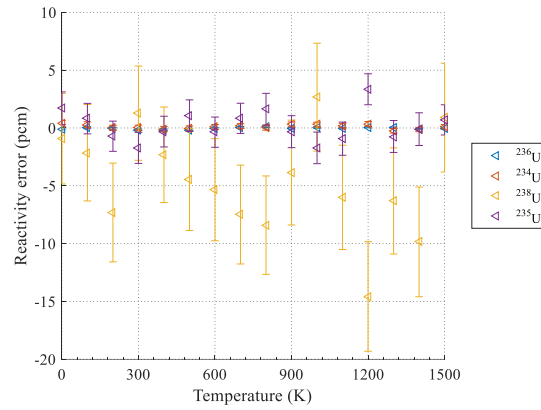


Figure 18. Isotope-wise reactivity error for pin 1C at 0.00 MWd/kgHM.

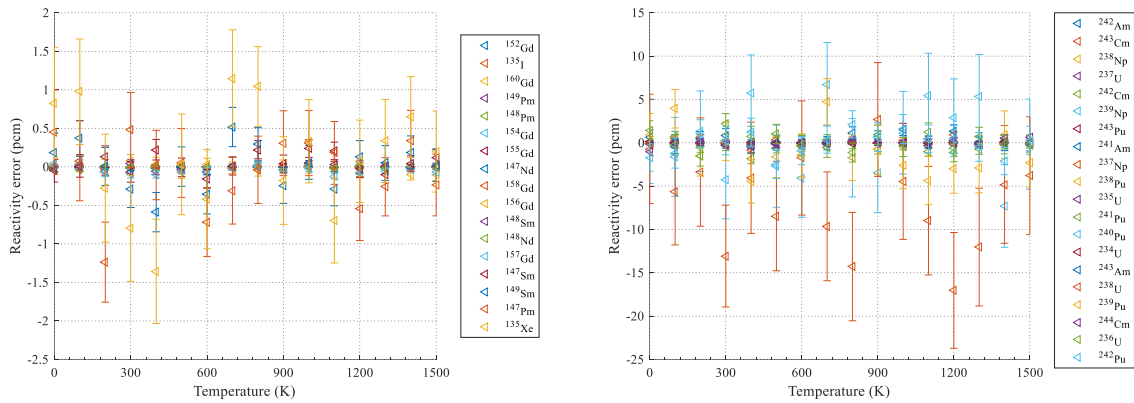


Figure 19. Isotope-wise reactivity error for pin 1C at 60.00 MWd/kgHM.

Similar reactivity errors are obtained for the 1I problem, which includes the Gd_2O_3 burnable poison within it, at 0.00 and 60.00 MWd/kgHM burnups at different temperatures in **Figure 20** and **Figure 21**, respectively. Although the errors for several isotopes are of several tens of pcm in the fresh fuel pin case, all the isotope-wise reactivity errors are within three standard deviations.

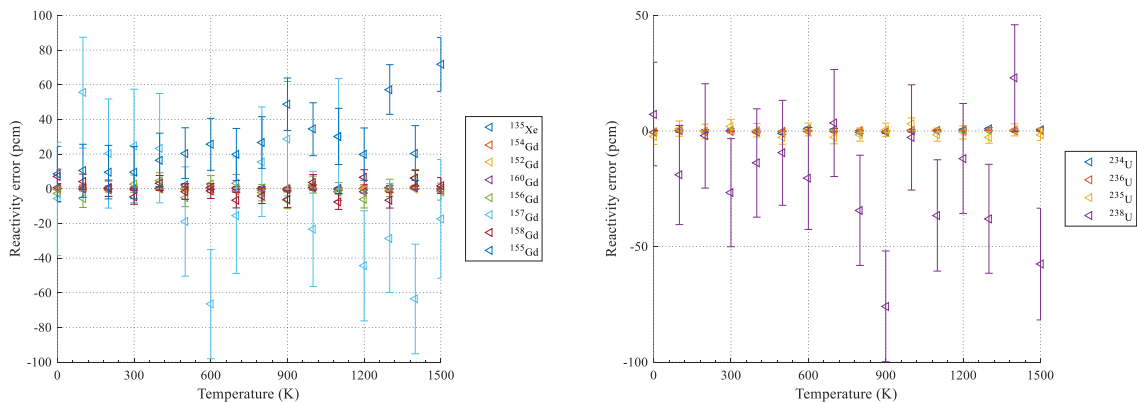


Figure 20. Isotope-wise reactivity error for pin 1I at 0.00 MWd/kgHM.

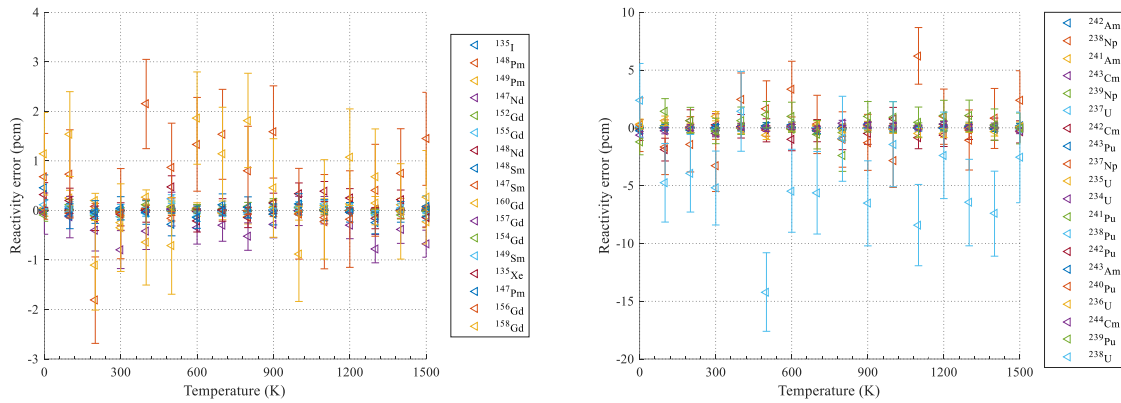


Figure 21. Isotope-wise reactivity error for pin 1I at 60.00 MWd/kgHM.

In addition, the absorption and fission reaction rates of the selected nuclides are compared. **Figure 22** and **Figure 23** illustrate the relative differences of those reaction rates for 1C pin problem at 0.00 and 60.00 MWd/kgHM burnups, respectively. The absorption reaction rate errors do not exceed 0.3 %, and the fission reaction rate differences are less than 0.15 % for both fresh and burned 1C fuel pin. Absorption and fission reaction rate comparisons between the ACE and WMP libraries for the fresh and burned 1I pin-cell problem are given in **Figure 24** and **Figure 25**, respectively. The results for the selected nuclides show similar behavior as in problem 1C.

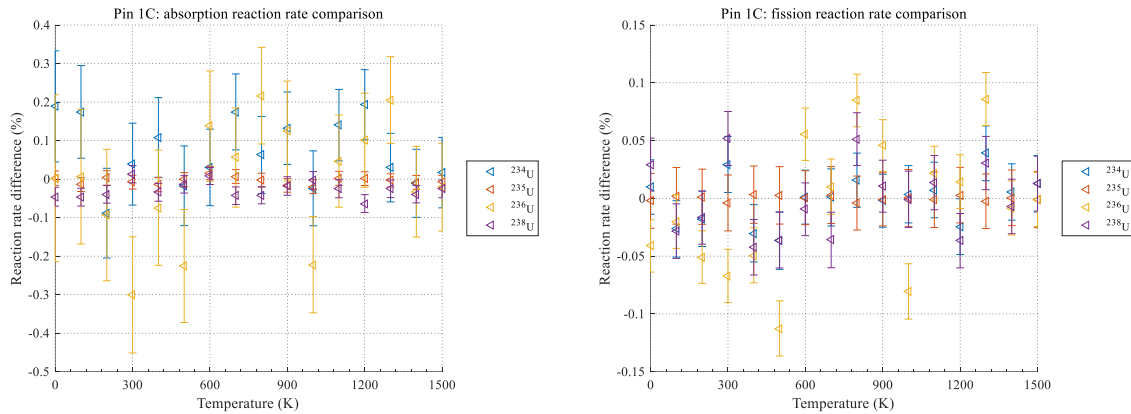


Figure 22. Isotope-wise reaction rate difference for pin 1C at 0.00 MWd/kgHM.

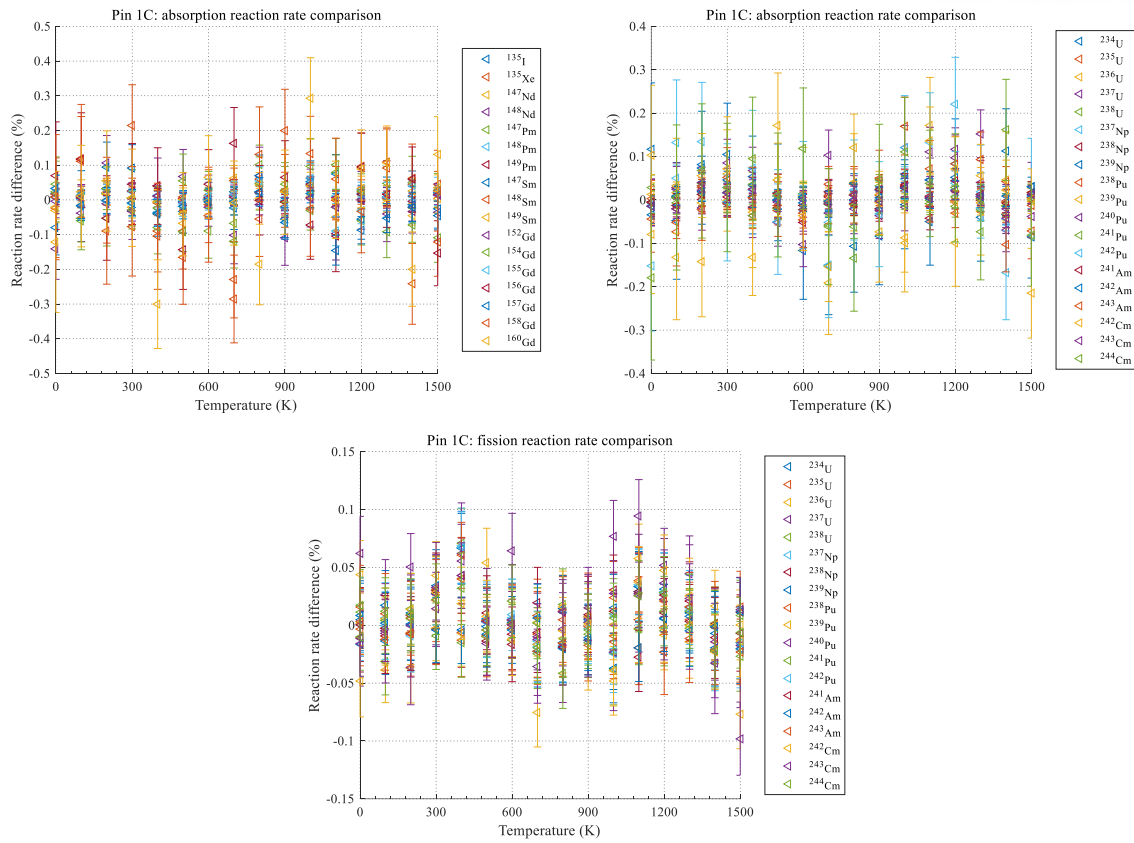


Figure 23. Isotope-wise reaction rate differences for pin 1C at 60.00 MWd/kgHM.

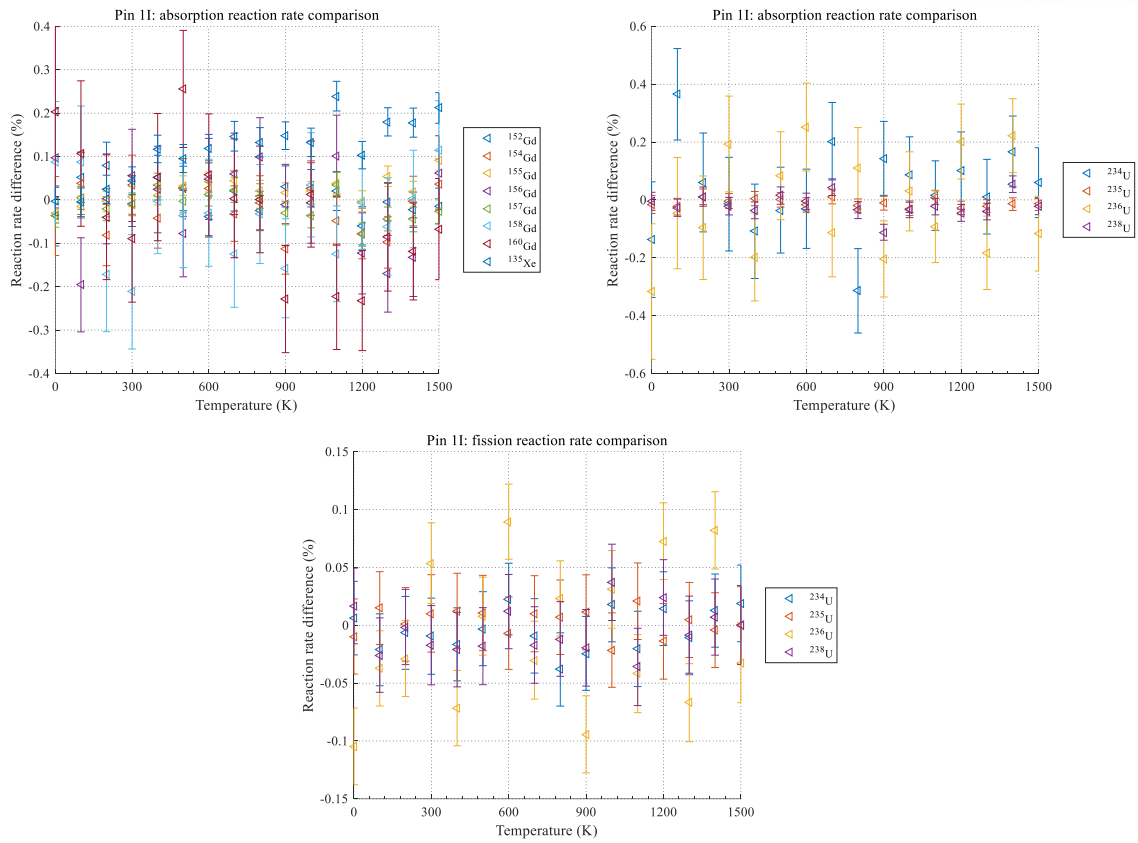


Figure 24. Isotope-wise reaction rate differences for pin 1I at 0.00 MWd/kgHM.

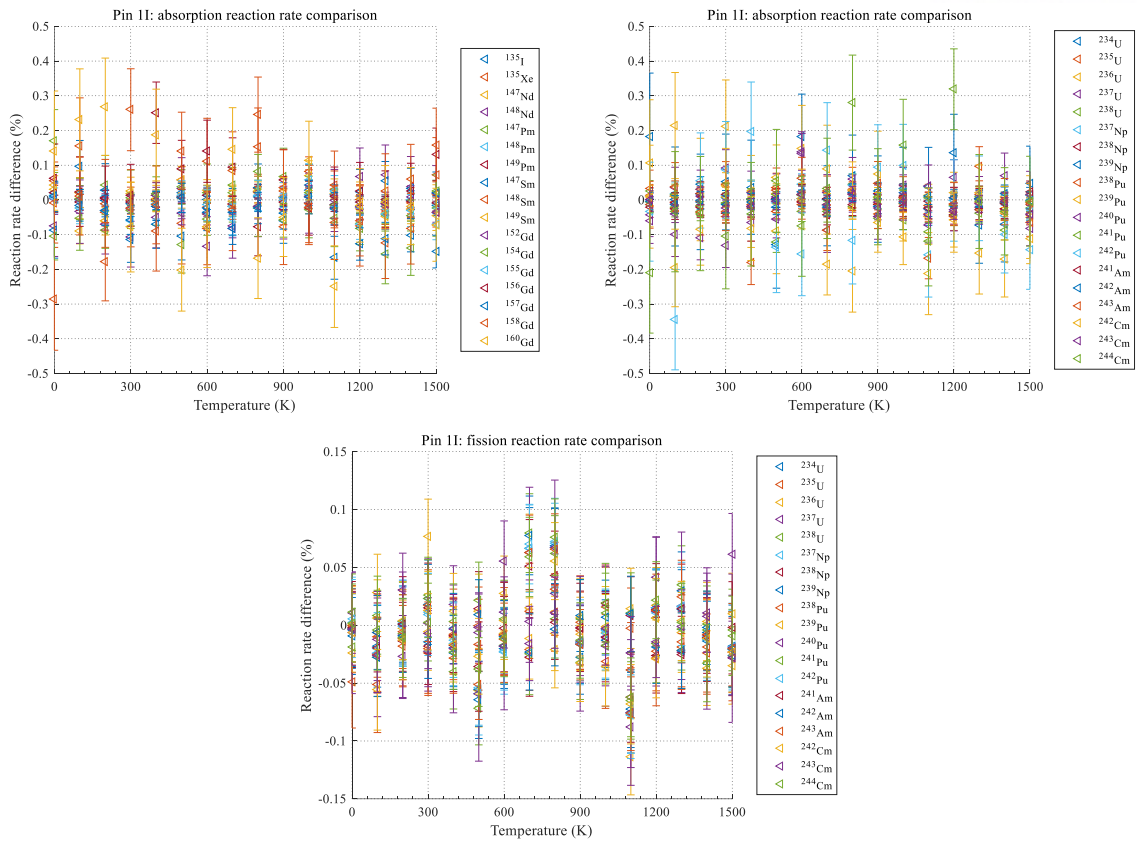


Figure 25. Isotope-wise reaction rate differences for pin 1I at 60.00 MWd/kgHM.

5.2 PWR Fuel Assembly

In the case of the fuel assembly simulations, the VERA benchmark provides 15 problems including four fuel enrichments, three temperature configurations, four burnable poison types, and two control rod materials. **Table 7** summarizes all the fuel assembly problems given in the VERA benchmark suite. Four assemblies to test WMP library are selected: 2C, 2F, 2G, and 2P with no poison, pyrex, AIC, and Gadolinia, respectively.

Table 7. VERA single fuel assembly depletion benchmark problems.

Problem	Description	Temperature (K)			²³⁵ U wt.%
		Moderator	Cladding	Fuel	
2A	FA (No poison)	565	565	565	3.1
2B	FA (No poison)	600	600	600	3.1
2C	FA (No poison)	600	600	900	3.1
2D	FA (No poison)	600	600	1200	3.1
2E	FA (12 Pyrex)	600	600	900	3.1
2F	FA (24 Pyrex)	600	600	900	3.1
2G	FA (24 AIC)	600	600	900	3.1
2H	FA (24 B ₄ C)	600	600	900	3.1
2I	FA (IT, Instrumentation Tube)	600	600	900	3.1
2J	FA (IT, 24 pyrex)	600	600	900	3.1
2K	FA (Zoned, 24 pyrex)	600	600	900	3.1/3.6
2L	FA (80 IFBA)	600	600	900	3.1
2M	FA (128 IFBA)	600	600	900	3.1
2N	FA (104 IFBA, 20 WABA)	600	600	900	3.1
2O	FA (12 Gadolinia)	600	600	900	3.1/1.8
2P	FA (24 Gadolinia)	600	600	900	3.1/1.8

Monte Carlo simulations for the selected fuel assembly problems are performed using 200 inactive, and 200 active cycles with 1,000,000 neutrons per cycle. The multiplication factor comparison between the ACE and WMP libraries are shown in **Table 8**.

Table 8. Selected VERA single fuel assembly problems multiplication factor comparison.

FA problem	ACE		WMP	
	k_{inf}	STD	k_{inf}	STD
2C	1.17367	0.00007	1.17361	0.00007
2F	0.97534	0.00006	0.97539	0.00007
2G	0.84729	0.00006	0.84747	0.00007
2P	0.92661	0.00007	0.92666	0.00006

The normalized pin power distributions are compared for Monte Carlo simulation between the ACE cross sections and the WMP library for the chosen VERA fuel assembly problems. **Figure 26-Figure 29** illustrates the absolute difference and corresponding standard deviations of the pin power for assemblies 2C, 2F, 2G, and 2P, respectively. It is obvious from the results below that pin power error is always less than 0.5 % due to the introduction of the WMP library instead of the conventional ACE cross sections.

FA 2C: pin power comparison between ACE vs. WMP

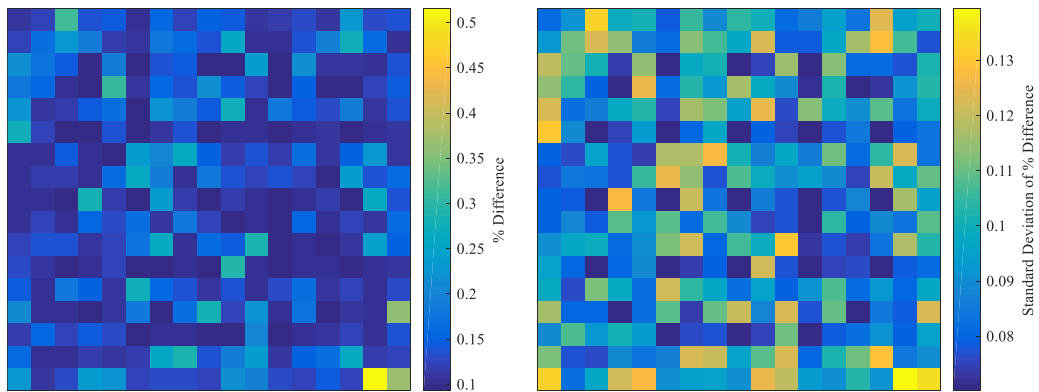


Figure 26. FA 2C: Relative pin power difference between ACE and WMP.

FA 2F: pin power comparison between ACE vs. WMP

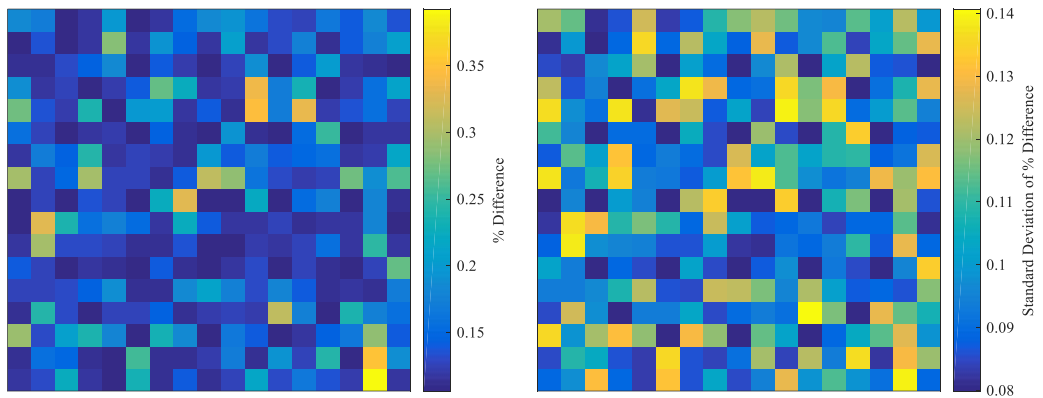


Figure 27. FA 2F: Relative pin power difference between ACE and WMP.

FA 2G: pin power comparison between ACE vs. WMP

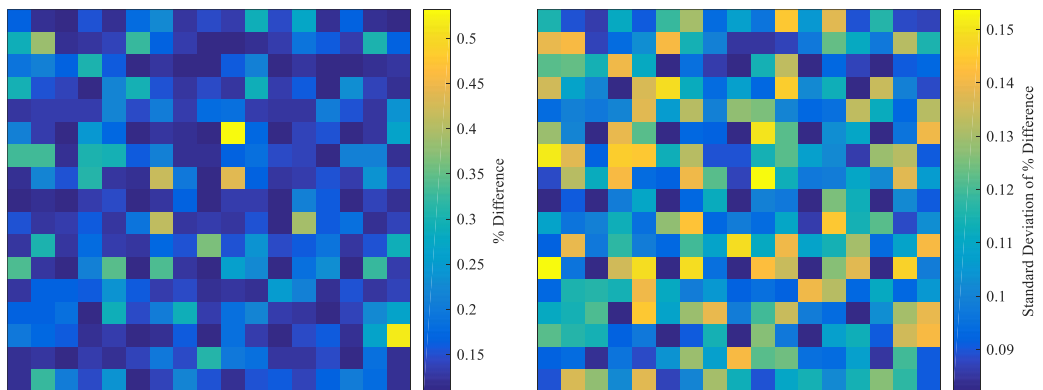


Figure 28. FA 2G: Relative pin power difference between ACE and WMP.

FA 2P: pin power comparison between ACE vs. WMP

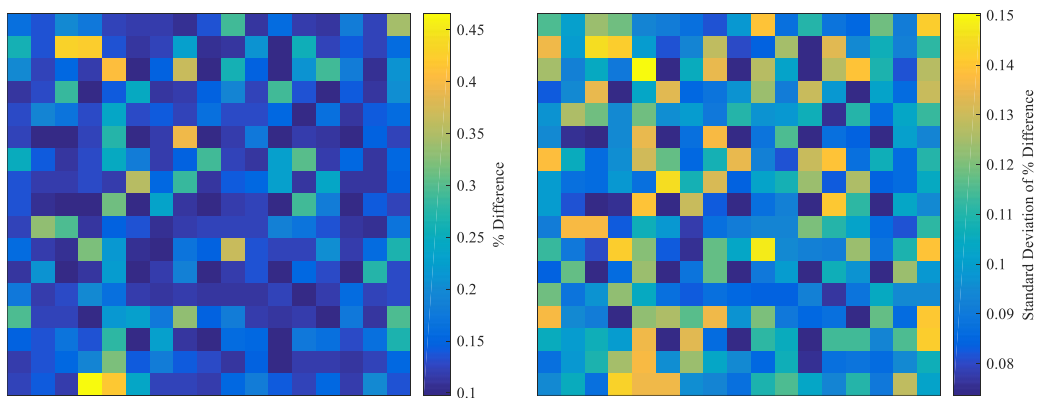


Figure 29. FA 2P: Relative pin power difference between ACE and WMP.

5.3 Performance Tests

In Sections 5.1, and 5.2 the application of the in-house generated windowed multipole library is presented for the VERA benchmark suite selected fuel pin and assembly problems, respectively. The multiplication factor, number density, isotope-wise reactivity, reaction rates, and pin power comparisons are given. This section provides the performance tests result in terms of clock cycles for the WMP library application in on-the-fly Doppler broadening. The convergence of the solution is not a priority in the performance evaluation tests; hence, the number of cycles and particles per cycle are significantly reduced. **Table 9** presents the number of inactive and active cycles, as well as the particle number per cycle used in the given tests.

Table 9. Performance tests: Monte Carlo simulation configurations.

Parameter	Value
Number of inactive cycles	100
Number of active cycles	200
Number of neutrons per cycle	500

The Monte Carlo code MCS contains a subroutine `get_xs_micro_all`, which provides all the reaction cross section types during the simulation. Within the given function, the temperature dependent cross sections are from the ACE file, or the windowed multipole reconstruction routine. The clock cycles are estimated per call of the `get_xs_micro_all` subroutine. **Table 10** shows the clock cycle comparison of the single temperature ACE cross section utilization and on-the-fly Doppler broadening routine with the in-house generated WMP library. Although the ACE cross section lookup time decreased by 45 %, the overall performance of the `get_xs_micro_all` subroutine decreases by 58 % due to on-the-fly cross section generation. The slowing down of the subroutine providing the cross section due to the WMP library translates into a 28% performance loss of the Monte Carlo simulation.

Table 10. Estimated clock cycles per `get_xs_micro_all` call (* indicates sub-function).

	ACE	WMP	Difference (%)
Total	568	897	58%
ACE cross section	84	46	-45%
Windowed Multipole cross section	-	284	-
* Faddeeva function evaluation	-	130	-
* Broadening of polynomial	-	5	-

VI. Conclusion and Future Work

This thesis presents the generation process of a windowed multipole library and its verification in the on-the-fly Doppler broadening routine of the UNIST in-house Monte Carlo code MCS. The re-processing of the conventional formalisms resonance parameters into rigorous multipole parameters was performed. The reduction of the overall number multipole parameters was achieved through implementing pseudo poles, and the window concept. The latter technique allowed us to decrease the number of poles used in cross section reconstruction at a single energy point of the target temperature.

The verification of the generated WMP library was achieved through solving selected VERA benchmark suite pin-cell and fuel assembly problems using the Monte Carlo code MCS. The multiplication factor, isotope-wise reactivity error, absorption and fission reaction rates comparison at the different temperatures were evaluated for fresh and burned fuel pins. In the case of the assembly problems, pin power differences were calculated for the ACE and WMP libraries not exceeding 0.5 %. In addition to accuracy tests, the performance of the in-house generated WMP library was evaluated. Although the cross section generation time increased by around 50 %, the Monte Carlo simulation performance loss was only about 30 %.

Throughout the given research, the in-house converting capability from Breit-Wigner, and Reich-Moore formalisms into a rigorous multipole representation, and its further optimization into a windowed multipole library were achieved. In the future, the isotopes with no resonance data need to be re-processed into the windowed multipole library, as well as converting and optimizing the most recent version of the ENDF/B-VIII.0 neutron induced data.

APPENDIX A

LEVEL MATRIX

Table 11 shows the Breit-Wigner resonance parameters of ^{78}Kr isotope (ENDF/B-VII.1) are used to reconstruct the level matrix for Breit-Wigner formalisms. According to the table given below, there are in total four resonances, meaning that the size of the level matrix is 4×4 . Recall, the level matrix is diagonal, and elements are given in Eq. (28).

Table 11. Breit-Wigner s-wave resonance parameters.

E_λ	l	J	$\Gamma_{\lambda t}$	$\Gamma_{\lambda n}$	$\Gamma_{\lambda \gamma}$	$\Gamma_{\lambda f}$
-122.0000	0	0.50	1.19500	0.96000	0.23500	0.00000
108.4000	0	0.50	0.28500	0.04900	0.23600	0.00000
450.9000	0	0.50	0.46600	0.23000	0.23600	0.00000
640.0000	0	0.50	1.73600	1.50000	0.23600	0.00000

As an example, the level matrix is calculated at 1 eV energy point. Since all the resonances are s-wave types, the level shift is zero according to Eq. (31). In addition, in order to simplify the problem, the energy dependence of the neutron half-width is ignored. The numerical values of the level matrix elements are given in Eq. (76), below.

$$A = \begin{bmatrix} -123.0 - 1.2i & -i0.5 & -i0.7 & -i1.4 \\ -i0.5 & 107.4 - 0.3i & -i0.3 & -i0.5 \\ -i0.7 & -i0.3 & 449.9 - i0.5 & -i0.8 \\ -i1.4 & -i0.5 & -i0.8 & 639.0 - i1.7 \end{bmatrix}, \quad (76)$$

Following the converting process given in the Section 3.1, it is possible to obtain the set of poles and residues of ^{78}Kr isotope. **Table 12** shows the numerical values of the calculated poles and residues corresponding to the each resonance energy. The given isotope does not have fission cross section, the residues corresponding to the reaction are zero and hence not included in the table, below. As soon as the rigorous multipole parameters are obtained, the window multipole library is generated following the instructions in Chapter IV. The WMP library for the ^{78}Kr isotope only contains poles and residues in **bold**, shown in **Table 12**. The windowed multipole library for the given isotope consists of only three poles, forty windows, and the fifth order polynomial. The information on the WMP library for the other isotopes are included in **Table 15**.

Table 12. Calculated poles and residues for ^{78}Kr isotope.

E_λ	$\text{Re}(d)$	$\text{Im}(d)$	$\text{Re}(R')$	$\text{Im}(R')$
-122.0000	0.005319	-11.067112	5.8170E+04	-5.4997E-02
	-0.005319	11.023655	5.7941E+04	5.4997E-02
108.4000	10.411534	-0.006843	3.1436E+03	-3.5525E-01
	-10.411534	0.004490	3.1436E+03	3.5525E-01
450.9000	21.234406	-0.005486	7.2350E+03	-9.2263E-01
	-21.234406	0.000071	7.2350E+03	9.2263E-01
640.0000	25.298217	-0.017155	3.9605E+04	-2.3206E+01
	-25.298217	-0.012491	3.9605E+04	2.3206E+01
E_λ	$\text{Re}(R^{\text{int}})$	$\text{Im}(R^{\text{int}})$	$\text{Re}(R^a)$	$\text{Im}(R^a)$
-122.0000	7.5321E+01	2.2592E-03	3.2822E+03	1.3408E+04
	-7.4916E+01	-2.5026E-03	3.2822E+03	-1.3408E+04
108.4000	3.7144E-02	-7.6611E+00	2.6032E+03	1.0524E-07
	1.5576E-02	7.6612E+00	3.9674E+03	-1.0524E-07
450.9000	3.1282E-01	2.2752E+01	3.6641E+03	1.5797E-08
	1.6457E-01	-2.2753E+01	2.8458E+05	-1.5797E-08
640.0000	4.4273E-01	-1.8054E+02	5.3841E+03	1.9722E-07
	2.5426E-01	1.8054E+02	-7.3947E+03	-1.9722E-07

CHANNEL MATRIX

In order to reconstruct the channel matrix, the Reich-Moore resonance parameters for ^{241}Pu isotope are obtained from ENDF/B-VII.1 neutron incident library. For the given isotope there are 244 s-wave resonances. **Table 13** shows only the first four resonances for compound nucleus $J = 2$.

Table 13. Reich-Moore s-wave resonance parameters.

E_λ	l	J	$\Gamma_{\lambda n}$	$\Gamma_{\lambda \gamma}$	$\Gamma_{\lambda fa}$	$\Gamma_{\lambda fb}$
-59.5300	0.0000	2.0000	0.5961	0.0445	0.4153	0.0430
0.1501	0.0000	2.0000	3.84E-07	0.0423	0.0200	0.0200
1.7253	0.0000	2.0000	2.07E-06	0.0403	0.0679	0.2823
4.5873	0.0000	2.0000	0.0005	0.0368	-0.0192	0.1211

The channel matrix elements are generated using the Reich-Moore formatted resonance parameters given for $l=0$ and $J=2$. There are 110 resonance levels for ^{241}Pu isotope with the given quantum numbers. The expressions for channel matrix elements are given in Eq. (46). There are neutrons, and first and second partial fission channels for RM formalism. Hence, in the case of the

fissile isotopes the size of the channel matrix is 3x3. Eq. (77) illustrates the elements of the channel matrix calculated at 1 eV.

$$(I - K) = \begin{bmatrix} 1.00 - i1.22 \times 10^{-4} & -1.18 \times 10^{-5} + i2.47 \times 10^{-7} & 2.95 \times 10^{-5} - i4.68 \times 10^{-3} \\ -1.18 \times 10^{-5} + i2.47 \times 10^{-7} & 1.00 - i0.44 & 2.61 \times 10^{-3} - i3.98 \times 10^{-2} \\ 2.95 \times 10^{-5} - i4.68 \times 10^{-3} & 2.61 \times 10^{-3} - i3.98 \times 10^{-2} & 1.01 - i0.32 \end{bmatrix}, \quad (77)$$

The RM formatted resonance parameters are converted into rigorous multipoles using the process described in Section 3.2. **Table 14** shows the generated poles and residues using the Reich-Moore resonance parameters of ²⁴¹Pu isotope, including only first four levels. The WMP library contains 244 poles, 60 windows, and the 6th order polynomial coefficients for the given isotope. The windowed multipole library is generated following Chapter IV.

Table 14. Calculated poles and residues for ²⁴¹Pu isotope.

E_λ	$\text{Re}(d)$	$\text{Im}(d)$	$\text{Re}(R^i)$	$\text{Im}(R^i)$
-59.53	1.61752E-02	-7.73301E+00	2.12264E+04	1.48578E+02
	-1.59067E-02	7.69440E+00	2.10122E+04	1.45199E+02
0.1501	3.97766E-01	-4.93081E-02	2.32946E-01	1.60131E-01
	-3.97765E-01	4.93077E-02	2.32917E-01	1.60204E-01
1.7253	1.32518E+00	-7.20455E-02	-4.29071E-01	1.18089E+00
	-1.32518E+00	7.20463E-02	-4.29606E-01	1.18085E+00
4.5873	2.14576E+00	-1.80601E-02	4.52720E+01	2.43771E+01
	-2.14572E+00	1.79772E-02	4.53659E+01	2.43045E+01
E_λ	$\text{Re}(R^a)$	$\text{Im}(R^a)$	$\text{Re}(R^f)$	$\text{Im}(R^f)$
-59.53	8.62539E+03	1.05294E+04	7.84945E+03	9.59555E+03
	8.62541E+03	-1.02356E+04	7.84947E+03	-9.30179E+03
0.1501	2.32922E-01	1.60164E-01	8.07407E-02	1.59578E-01
	2.32941E-01	1.60172E-01	8.07534E-02	1.59587E-01
1.7253	-4.29314E-01	1.18067E+00	-5.55464E-01	1.18846E+00
	-4.29364E-01	1.18108E+00	-5.55531E-01	1.18887E+00
4.5873	4.51313E+01	2.43192E+01	3.33614E+01	2.43028E+01
	4.55076E+01	2.43624E+01	3.36664E+01	2.43459E+01

APPENDIX B

Table 15. List of isotopes with WMP library generated from ENDF/B-VII.1.

Isotope	Upper Limit (eV)	WMP library			[RMP time / WMP time] per energy point	
		# of poles	# of windows	fit order	at 0 K	at 300 K
²⁵ Mg	2.20E+05	8	392	2	8	198
²⁶ Mg	4.50E+05	5	800	2	6	184
²⁷ Al	8.45E+05	89	403	2	31	250
²⁸ Al	1.75E+06	49	175	2	20	231
²⁹ Al	1.30E+06	26	130	2	12	234
³⁰ Al	1.50E+06	28	324	2	13	218
³² S	1.57E+06	121	157	3	42	231
³³ S	2.60E+05	8	26	4	5	138
³⁴ S	4.80E+05	9	11	5	7	185
³⁷ Cl	1.20E+06	310	2400	2	2	19
³⁶ Ar	4.65E+04	4	1860	5	3	189
³⁸ Ar	3.00E+05	4	1500	5	3	182
⁴⁰ Ar	1.50E+06	436	1498	3	2	10
⁴¹ K	1.00E+06	694	1000	5	2	9
⁴⁰ Ca	5.00E+05	146	233	2	82	275
⁴² Ca	3.00E+05	40	300	2	24	201
⁴³ Ca	4.00E+04	26	187	2	11	179
⁴⁴ Ca	5.00E+05	39	50	4	17	167
⁴⁸ Ca	5.00E+05	6	24	4	6	183
⁴⁵ Sc	9.69E+04	606	1552	2	2	7
⁴⁶ Ti	3.63E+05	108	169	2	57	198
⁴⁷ Ti	7.49E+04	37	162	2	14	173
⁴⁸ Ti	4.00E+05	119	400	2	39	227
⁴⁹ Ti	2.41E+05	183	1122	3	28	180
⁵⁰ Ti	5.87E+05	34	274	2	21	243
⁵⁰ V	4.25E+04	17	92	4	7	148
⁵¹ V	1.00E+05	66	216	2	33	189
⁵⁰ Cr	7.83E+05	396	435	4	103	257
⁵² Cr	1.43E+06	340	2554	4	118	480
⁵³ Cr	5.64E+05	346	564	4	104	238
⁵⁴ Cr	8.34E+05	117	464	2	36	219
⁵⁵ Mn	1.25E+05	164	224	4	48	203
⁵⁴ Fe	7.00E+05	238	2188	2	113	315
⁵⁶ Fe	8.50E+05	313	1518	2	89	319
⁵⁷ Fe	2.00E+05	72	625	4	27	262
⁵⁸ Fe	4.00E+05	67	4000	2	25	425
⁵⁹ Co	1.00E+05	334	800	5	2	9
⁵⁸ Ni	8.12E+05	494	1450	2	138	485
⁶⁰ Ni	8.00E+05	462	800	2	125	359
⁶¹ Ni	5.70E+04	53	123	3	24	169
⁶² Ni	6.00E+05	79	600	3	42	213
⁶⁴ Ni	5.53E+05	63	56	4	29	174
⁶³ Cu	9.95E+04	222	463	3	67	191
⁶⁵ Cu	9.95E+04	156	995	3	54	200
⁷⁰ Zn	2.10E+05	108	560	3	66	254
⁶⁹ Ga	4.50E+03	25	74	5	13	156
⁷¹ Ga	5.60E+03	29	92	5	12	195
⁷⁰ Ge	1.40E+04	48	1400	10	1	18
⁷² Ge	1.20E+04	12	160	2	8	169
⁷³ Ge	8.63E+03	48	116	4	15	133

Continued on the next page

Table 15. Continued from the previous page.

Isotope	Upper Limit (eV)	WMP library			[RMP time/ WMP time] per energy point	
		# of poles	# of windows	fit order	at 0K	at 300K
⁷⁴ Ge	6.00E+03	4	114	7	5	140
⁷⁶ Ge	3.00E+04	8	214	7	5	131
⁷⁴ As	5.50E+01	3	11	5	3	118
⁷⁵ As	3.00E+04	8	214	7	5	131
⁷⁴ Se	2.60E+03	7	260	5	6	166
⁷⁶ Se	9.00E+03	18	128	8	10	158
⁷⁷ Se	2.70E+03	32	67	8	15	140
⁷⁸ Se	1.20E+04	13	171	8	10	162
⁸⁰ Se	1.00E+04	9	143	7	8	173
⁸² Se	3.00E+04	6	285	4	6	175
⁷⁹ Br	5.50E+03	200	91	9	82	135
⁸¹ Br	1.60E+04	190	171	7	79	171
⁷⁸ Kr	8.00E+02	3	40	5	3	190
⁸⁰ Kr	1.00E+03	3	50	5	6	133
⁸² Kr	4.00E+01	1	4	5	3	132
⁸³ Kr	2.72E+02	2	19	7	3	132
⁸⁴ Kr	9.00E+04	57	480	4	36	198
⁸⁵ Kr	1.80E+03	7	45	8	4	125
⁸⁵ Rb	8.47E+03	141	91	5	122	212
⁸⁶ Rb	3.00E+03	65	74	7	28	140
⁸⁷ Rb	1.25E+04	11	178	8	12	174
⁸⁴ Sr	3.40E+03	10	73	8	6	157
⁸⁶ Sr	3.00E+04	32	285	9	18	161
⁸⁷ Sr	1.41E+04	115	232	5	32	145
⁸⁸ Sr	3.00E+05	87	1600	2	49	292
⁸⁹ Y	4.50E+04	41	320	7	204	361
⁹⁰ Y	1.00E+04	33	134	3	19	164
⁹⁰ Zr	5.35E+04	23	54	2	13	166
⁹¹ Zr	1.00E+04	50	218	2	26	154
⁹² Zr	7.10E+04	71	331	2	56	220
⁹³ Zr	6.80E+03	51	136	3	26	163
⁹⁴ Zr	9.00E+04	72	419	2	37	201
⁹⁶ Zr	1.00E+05	29	100	3	15	159
⁹³ Nb	7.35E+03	193	613	5	63	254
⁹⁴ Nb	2.80E+01	2	8	5	3	119
⁹² Mo	4.00E+04	59	400	2	35	185
⁹⁴ Mo	2.00E+04	54	112	3	31	166
⁹⁵ Mo	2.14E+03	56	343	5	29	203
⁹⁶ Mo	1.90E+04	72	1056	2	44	194
⁹⁷ Mo	2.00E+03	66	200	2	30	146
⁹⁸ Mo	3.20E+04	142	696	3	79	215
¹⁰⁰ Mo	2.60E+04	122	260	4	60	227
⁹⁹ Tc	6.38E+03	535	158	5	143	138
⁹⁹ Ru	1.00E+03	40	50	5	12	102
¹⁰⁰ Ru	1.20E+04	87	198	4	46	175
¹⁰¹ Ru	1.04E+03	48	52	7	14	103
¹⁰² Ru	1.34E+04	144	166	3	62	187
¹⁰³ Ru	3.50E+02	8	35	8	4	108
¹⁰⁴ Ru	1.11E+04	109	183	3	47	203
¹⁰³ Rh	4.17E+03	707	209	5	22	37
¹⁰⁵ Rh	7.50E+00	1	4	10	3	113
¹⁰² Pd	8.20E+02	3	41	5	3	131
¹⁰⁴ Pd	7.50E+03	122	160	8	61	180
¹⁰⁵ Pd	2.05E+03	198	68	5	54	105

Continued on the next page

Table 15. Continued from the previous page.

Isotope	Upper Limit (eV)	WMP library			[RMP time/ WMP time] per energy point	
		# of poles	# of windows	fit order	at 0 K	at 300 K
¹⁰⁶ Pd	6.00E+03	85	99	6	46	163
¹⁰⁷ Pd	1.00E+03	63	50	5	36	100
¹⁰⁸ Pd	5.50E+03	214	136	5	23	98
¹¹⁰ Pd	6.80E+03	79	112	5	40	167
¹⁰⁷ Ag	6.50E+03	400	1161	2	136	184
¹⁰⁹ Ag	7.12E+03	449	223	10	139	151
¹¹¹ Ag	9.99E+02	82	50	6	30	115
¹¹⁰ Ag-m	1.25E+02	10	7	8	5	104
¹⁰⁶ Cd	6.00E+03	56	600	2	19	167
¹⁰⁸ Cd	6.00E+03	65	600	2	20	161
¹¹⁰ Cd	7.00E+03	91	700	3	30	161
¹¹¹ Cd	2.30E+03	155	1070	2	42	130
¹¹² Cd	1.15E+04	118	1150	2	34	157
¹¹³ Cd	5.00E+03	592	500	8	29	62
¹¹⁴ Cd	8.00E+03	79	800	2	26	165
¹¹⁶ Cd	9.50E+03	47	4419	2	17	185
¹¹⁵ Cd-m	1.00E+03	24	50	7	12	149
¹¹³ In	6.00E+02	125	108	4	22	101
¹¹⁵ In	2.00E+03	626	358	4	75	116
¹¹² Sn	1.50E+03	15	150	2	8	153
¹¹³ Sn	5.10E+02	29	34	7	15	133
¹¹⁴ Sn	2.00E+03	13	94	2	9	161
¹¹⁵ Sn	9.00E+02	5	42	4	3	131
¹¹⁶ Sn	3.00E+04	213	300	3	101	222
¹¹⁷ Sn	2.30E+03	76	230	2	30	128
¹¹⁸ Sn	2.00E+03	8	94	2	8	159
¹¹⁹ Sn	1.26E+03	23	126	3	11	146
¹²⁰ Sn	5.00E+04	223	500	3	131	279
¹²² Sn	3.00E+05	354	647	3	163	325
¹²⁴ Sn	3.15E+05	190	315	4	89	207
¹²⁵ Sn	9.90E+02	9	49	10	7	142
¹²¹ Sb	5.40E+03	213	134	5	48	99
¹²³ Sb	5.40E+03	204	134	6	61	135
¹²⁶ Sb	9.99E+02	99	67	6	32	105
¹²² Te	2.00E+04	750	62	6	35	69
¹²³ Te	2.00E+03	43	400	4	14	155
¹²⁴ Te	1.50E+04	186	160	8	81	198
¹²⁵ Te	7.75E+03	293	128	7	128	183
¹²⁶ Te	1.36E+04	57	146	5	30	175
¹²⁸ Te	2.25E+04	38	240	6	22	174
¹³⁰ Te	3.10E+04	22	331	7	15	175
¹³² Te	2.78E+04	26	297	5	17	186
¹²⁷ I	4.05E+03	339	100	4	89	120
¹²⁹ I	3.40E+03	124	84	7	42	138
¹³⁰ I	5.60E+02	63	38	6	23	114
¹²⁴ Xe	2.60E+02	6	208	5	3	156
¹²⁶ Xe	2.33E+03	4	104	4	3	131
¹²⁸ Xe	3.50E+03	14	88	3	7	126
¹²⁹ Xe	4.10E+03	69	103	4	19	112
¹³⁰ Xe	4.00E+03	18	100	4	7	135
¹³¹ Xe	3.95E+03	47	132	4	14	123
¹³² Xe	4.00E+03	6	100	3	4	137
¹³⁴ Xe	1.00E+04	5	165	3	6	184
¹³⁵ Xe	1.90E+02	2	608	2	2	78

Continued on the next page

Table 15. Continued from the previous page.

Isotope	Upper Limit (eV)	WMP library			[RMP time/ WMP time] per energy point	
		# of poles	# of windows	fit order	at 0 K	at 300 K
¹³⁶ Xe	4.90E+05	36	1307	3	23	254
¹³³ Cs	4.00E+03	214	134	4	56	104
¹³⁴ Cs	1.80E+02	7	24	4	4	119
¹³⁵ Cs	2.20E+02	6	22	4	4	119
¹³⁰ Ba	2.80E+03	51	560	2	14	122
¹³² Ba	1.30E+02	2	26	2	3	131
¹³³ Ba	3.06E+02	6	31	3	4	125
¹³⁴ Ba	1.10E+04	86	182	3	42	178
¹³⁵ Ba	4.70E+03	110	118	3	34	141
¹³⁶ Ba	3.50E+04	103	374	9	52	198
¹³⁷ Ba	1.25E+04	77	206	3	36	189
¹³⁸ Ba	1.40E+05	33	1120	5	21	196
¹⁴⁰ Ba	2.30E+04	8	1840	5	5	144
¹³⁸ La	3.30E+02	9	33	4	5	104
¹³⁹ La	2.00E+04	277	500	2	35	120
¹⁴⁰ La	9.99E+02	15	67	3	6	122
¹³⁶ Ce	8.80E+02	13	59	3	5	125
¹³⁸ Ce	9.99E+02	8	50	4	5	132
¹³⁹ Ce	3.01E+02	9	27	5	5	120
¹⁴⁰ Ce	2.00E+05	166	1235	2	108	298
¹⁴¹ Ce	3.50E+02	6	35	4	4	148
¹⁴² Ce	1.30E+04	30	214	3	20	173
¹⁴³ Ce	4.60E+02	11	31	5	5	120
¹⁴¹ Pr	1.01E+04	188	166	4	73	175
¹⁴² Pr	9.99E+02	23	50	4	9	118
¹⁴³ Pr	3.75E+02	5	75	4	4	132
¹⁴² Nd	2.25E+04	71	279	4	35	180
¹⁴³ Nd	5.50E+03	149	138	5	44	144
¹⁴⁴ Nd	9.98E+03	136	399	3	27	173
¹⁴⁶ Nd	7.60E+03	56	190	2	29	171
¹⁴⁷ Nd	1.80E+02	11	24	5	5	100
¹⁴⁸ Nd	9.99E+03	114	220	3	45	162
¹⁵⁰ Nd	1.39E+04	77	228	3	24	153
¹⁴⁷ Pm	1.02E+02	22	21	5	13	89
¹⁵¹ Pm	1.56E+02	38	32	4	11	85
¹⁴⁸ Pm-m	1.00E+00	1	2000	2	3	235
¹⁴⁴ Sm	1.19E+04	74	299	2	40	181
¹⁴⁷ Sm	1.99E+03	212	100	5	44	83
¹⁴⁸ Sm	9.14E+02	15	366	2	5	133
¹⁴⁹ Sm	5.20E+02	217	416	5	21	40
¹⁵⁰ Sm	1.57E+03	32	79	4	8	110
¹⁵¹ Sm	2.96E+02	163	119	7	19	42
¹⁵² Sm	5.15E+03	91	172	5	25	133
¹⁵³ Sm	2.50E+01	12	50	3	5	97
¹⁵⁴ Sm	5.20E+03	35	260	2	12	126
¹⁵¹ Eu	1.00E+02	128	400	5	10	28
¹⁵² Eu	6.20E+01	83	62	4	20	63
¹⁵³ Eu	9.80E+01	71	14	7	16	67
¹⁵⁴ Eu	2.75E+01	35	550	2	3	38
¹⁵⁵ Eu	2.97E+01	11	297	2	4	95
¹⁵⁷ Eu	6.72E+01	21	12	7	7	82
¹⁵² Gd	2.66E+03	186	709	6	25	74
¹⁵³ Gd	1.32E+02	17	528	5	4	78
¹⁵⁴ Gd	2.76E+03	163	69	5	40	92

Continued on the next page

Table 15. Continued from the previous page.

Isotope	Upper Limit (eV)	WMP library			[RMP time/ WMP time] per energy point	
		# of poles	# of windows	fit order	at 0 K	at 300 K
¹⁵⁵ Gd	1.83E+02	117	367	6	14	49
¹⁵⁶ Gd	2.23E+03	88	99	3	25	124
¹⁵⁷ Gd	3.07E+02	61	614	6	16	114
¹⁵⁸ Gd	9.98E+03	95	220	3	25	140
¹⁶⁰ Gd	9.66E+03	57	242	2	18	152
¹⁵⁹ Tb	1.25E+03	222	84	4	47	80
¹⁶⁰ Tb	9.00E+00	7	1440	2	3	82
¹⁵⁶ Dy	9.10E+01	19	364	2	7	106
¹⁵⁸ Dy	8.62E+01	3	12	6	3	131
¹⁶⁰ Dy	2.01E+03	66	101	4	16	81
¹⁶¹ Dy	9.96E+02	253	50	5	44	53
¹⁶² Dy	4.85E+03	126	388	5	16	87
¹⁶³ Dy	9.97E+02	132	89	6	24	69
¹⁶⁴ Dy	7.00E+03	136	87	7	24	133
¹⁶⁵ Ho	1.25E+03	248	63	4	55	78
¹⁶⁶ Ho-m	6.50E+01	5	130	6	2	87
¹⁶² Er	2.50E+02	17	34	4	7	101
¹⁶⁴ Er	8.00E+02	18	54	4	7	114
¹⁶⁶ Er	5.00E+03	122	250	2	45	155
¹⁶⁷ Er	1.75E+03	392	350	5	24	32
¹⁶⁸ Er	1.50E+04	129	330	2	40	154
¹⁷⁰ Er	5.00E+03	62	100	5	42	166
¹⁶⁹ Tm	1.95E+03	193	98	4	43	88
¹⁷⁰ Tm	8.96E+01	13	24	4	5	103
¹⁷⁵ Lu	4.11E+02	100	42	4	27	74
¹⁷⁶ Lu	1.02E+02	73	1632	6	11	45
¹⁷⁴ Hf	1.68E+02	16	560	6	5	93
¹⁷⁶ Hf	7.00E+02	17	63	4	9	112
¹⁷⁷ Hf	5.10E+02	169	204	6	38	76
¹⁷⁸ Hf	1.60E+03	33	1280	2	9	117
¹⁷⁹ Hf	5.10E+02	92	51	4	27	89
¹⁸⁰ Hf	4.99E+03	62	250	2	62	197
¹⁸¹ Ta	3.30E+02	75	44	4	20	84
¹⁸² Ta	3.50E+01	14	560	2	3	57
¹⁸⁰ W	1.00E+02	5	20	4	4	122
¹⁸² W	4.50E+03	91	900	2	40	137
¹⁸³ W	2.20E+03	95	110	3	28	123
¹⁸⁴ W	4.00E+03	46	100	2	35	124
¹⁸⁶ W	8.50E+03	166	213	4	40	141
¹⁸⁵ Re	2.00E+03	484	100	4	76	70
¹⁸⁷ Re	2.00E+03	374	89	5	74	82
¹⁹¹ Ir	1.53E+02	46	31	5	12	74
¹⁹³ Ir	3.10E+02	39	62	5	12	94
¹⁹⁷ Au	5.00E+03	263	167	4	64	127
¹⁹⁶ Hg	1.03E+02	1	14	7	3	135
¹⁹⁸ Hg	4.59E+02	5	46	3	4	130
¹⁹⁹ Hg	9.68E+02	9	49	5	5	131
²⁰⁰ Hg	8.58E+03	4	215	2	4	143
²⁰¹ Hg	7.54E+02	7	101	2	4	130
²⁰² Hg	4.52E+03	2	201	2	3	153
²⁰³ Tl	1.89E+04	84	311	3	40	194
²⁰⁵ Tl	8.37E+04	115	689	2	60	223
²⁰⁴ Pb	5.00E+04	63	412	2	43	408
²⁰⁶ Pb	9.00E+05	379	2400	2	115	349

Continued on the next page

Table 15. Continued from the previous page.

Isotope	Upper Limit (eV)	WMP library			[RMP time/ WMP time] per energy point	
		# of poles	# of windows	fit order	at 0 K	at 300 K
²⁰⁷ Pb	4.75E+05	134	1462	2	46	259
²⁰⁹ Bi	1.00E+05	71	800	5	44	229
²²⁶ Ra	1.00E+03	45	134	5	9	77
²²⁹ Th	8.00E+00	21	2560	2	6	79
²³² Th	4.00E+03	912	134	5	166	121
²³¹ Pa	1.17E+02	201	1872	2	12	23
²³² Pa	2.10E+01	47	420	2	8	54
²³³ Pa	1.07E+02	91	22	7	19	49
²³³ U	6.00E+02	1026	600	5	30	18
²³⁴ U	1.50E+03	119	84	4	30	100
²³⁵ U	2.25E+03	3184	2250	6	522	147
²³⁶ U	1.50E+03	116	100	4	38	136
²³⁷ U	2.00E+02	44	20	7	12	74
²³⁸ U	2.00E+04	3321	2000	2	619	323
²³⁹ U	1.03E+02	42	28	5	13	81
²³⁶ Np	2.15E+01	38	1075	6	10	90
²³⁷ Np	5.00E+02	666	50	7	88	51
²³⁸ Np	6.65E+00	22	532	2	6	85
²³⁶ Pu	1.00E+01	6	1600	6	3	91
²³⁸ Pu	5.00E+02	53	1000	5	16	109
²³⁹ Pu	1.00E+03	539	2000	2	45	45
²⁴⁰ Pu	5.70E+03	395	1900	2	27	46
²⁴¹ Pu	3.00E+02	242	60	6	44	54
²⁴² Pu	9.23E+02	64	93	4	21	120
²⁴³ Pu	1.02E+02	40	21	5	11	80
²⁴⁴ Pu	2.90E+02	14	39	4	6	114
²⁴¹ Am	1.50E+02	194	300	6	43	65
²⁴² Am	1.00E+02	120	40	7	27	62
²⁴³ Am	2.50E+02	232	50	4	32	42
¹⁴² Am-m	4.30E+01	111	86	6	22	73
²⁴² Cm	2.75E+02	12	37	4	6	119
²⁴³ Cm	1.00E+02	106	27	5	20	52
²⁴⁴ Cm	1.00E+03	85	2000	4	17	106
²⁴⁵ Cm	1.00E+02	86	20	7	19	66
²⁴⁷ Cm	6.00E+01	43	24	7	11	72
²⁴⁸ Cm	1.50E+03	34	100	3	15	122
²⁵⁰ Cm	1.50E+02	8	600	2	4	134
²⁴⁹ Bk	6.00E+01	54	60	6	8	45
²⁴⁹ Cf	7.00E+01	48	24	6	13	70
²⁵⁰ Cf	1.00E+01	6	1000	5	3	112
²⁵¹ Cf	5.00E+00	4	20	5	3	103
²⁵² Cf	1.00E+03	36	67	5	11	105

References

1. Wigner, E. P., & Eisenbud, L. (1947). Higher Angular Momenta and Long Range Interaction in Resonance Reactions. *Physical Review*, 72(1), 29-41. doi:10.1103/physrev.72.29.
2. Lane, A. M., & Thomas, R. G. (1958). R-Matrix Theory of Nuclear Reactions. *Review of Modern Physics*, 30.
3. Kapur, P. L., & Peierls, R. (1938). The Dispersion Formula for Nuclear Reactions. *Proceedings of the Royal Society A: Mathematical, Physical and Engineering Sciences*, 166(925), 277-295. doi:10.1098/rspa.1938.0093.
4. Hwang, R. N. (2009). Resonance Theory in Reactor Applications. *Nuclear Computational Science*, 217-290. doi:10.1007/978-90-481-3411-3_5.
5. Hwang, R. N. (1987). A Rigorous Pole Representation of Multilevel Cross Sections and Its Practical Applications. *Nuclear Science and Engineering*, 96(3), 192-209. doi:10.13182/nse87-a16381.
6. Hwang, R. N. (1992). An Extension of the Rigorous Pole Representation of Cross Sections for Reactor Applications. *Nuclear Science and Engineering*, 111(2), 113-131. doi:10.13182/nse92-a23928.
7. Jammes, C., & Hwang, R. N. (2000). Conversion of Single- and Multilevel Breit-Wigner Resonance Parameters to Pole Representation Parameters. *Nuclear Science and Engineering*, 134(1), 37-49. doi:10.13182/nse00-a2098.
8. Cross-Section Evaluation Working Group (2005), ENDF-6 Format Manual: Data Formats and Procedures for the Evaluated Nuclear Data File ENDF/B-VI and ENDF/B-VII, ENDF-102, Brookhaven National Lab.
9. R. E. MacFarlane, D. W. Muir, R. M Boicourt, A. C. Kahler (2012), The NJOY Nuclear Data Processing System, Version 2012.
10. Cullen, D. E., & Weisbin, C. R. (1976). Exact Doppler Broadening of Tabulated Cross Sections. *Nuclear Science and Engineering*, 60(3), 199-229. doi:10.13182/nse76-1.
11. Forget, B., Xu, S., & Smith, K. (2014). Direct Doppler broadening in Monte Carlo simulations using the multipole representation. *Annals of Nuclear Energy*, 64, 78-85. doi:10.1016/j.anucene.2013.09.043.
12. Josey, C., Ducru, P., Forget, B., & Smith, K. (2016). Windowed multipole for cross section Doppler broadening. *Journal of Computational Physics*, 307, 715-727. doi:10.1016/j.jcp.2015.08.013.
13. Josey, C. (2015), Windowed multipole: an efficient Doppler broadening technique for Monte Carlo. Master's thesis, Massachusetts Institute of Technology.

14. Josey, C., Forget, B., & Smith, K. (2015). Windowed multipole sensitivity to target accuracy of the optimization procedure. *Journal of Nuclear Science and Technology*, 52(7-8), 987-992. doi:10.1080/00223131.2015.1035353.
15. Josey, C., Forget, B., & Smith, K. (2014). Efficiency and accuracy evaluation of the windowed multipole direct Doppler broadening method, in: Proceedings of PHYSOR 2014.
16. Ducru P. (2016). On Methods for Conversion of R-Matrix Resonance Parameters to Multi-Pole Formalism-Numerics of Algebraic Conversion, in: Proceedings of PHYSOR 2016.
17. Godfrey, A. T. (2014). VERA core physics benchmark progression problem specifications. *Consortium for Advanced Simulation of LWRs*.
18. Peng, X., Ducru, P., Liu, S., Forget, B., Liang, J., & Smith, K. (2018). Converting point-wise nuclear cross sections to pole representation using regularized vector fitting. *Computer Physics Communications*, 224, 52-62. doi:10.1016/j.cpc.2017.12.004.
19. Xu S. (2013). On-the-fly Doppler Broadening using Multipole Representation for Monte Carlo Simulations on Heterogeneous Clusters. Master's thesis, Massachusetts Institute of Technology.
20. Lee, H., Choi, S., & Lee, D. (2015). A Hybrid Monte Carlo/Method-of-Characteristics Method for Efficient Neutron Transport Analysis. *Nuclear Science and Engineering*, 180(1), 69-85. doi:10.13182/nse13-102.
21. Khassenov, A., Choi, S. Y., & Lee, D. J. (2014). Application of Energy Window Concept in Doppler Broadening of ^{238}U Cross Section, in: *KNS Fall Meeting, Pyeongchang, Korea*.
22. Khassenov, A., Choi, S., & Lee, D. (2015). On the Fly Doppler Broadening Using Multipole Representation, in: *KNS Spring Meeting, Jeju, Korea*.
23. Khassenov A., Choi S., Lee, H., Zhang, P., Zheng, Y. and Lee, D. (2015). Preliminary Performance Evaluation of On-the-Fly Doppler Broadening Capability for Monte Carlo Simulation in MCS, in: *7ICMSNSE 2015*.
24. Yu, J., Khassenov, A., Zhang, P., and Lee, D. (2017). On the Convergence Issue for Multi-Poles Conversion from Reich-Moore Formalism, in: *M&C 2017*.
25. Jang, J., Kim, W., Jeong, S., Jeong, E., Park, J., Lemaire, M., . . . Lee, D. (2018). Validation of UNIST Monte Carlo code MCS for criticality safety analysis of PWR spent fuel pool and storage cask. *Annals of Nuclear Energy*, 114, 495-509. doi:10.1016/j.anucene.2017.12.054.

Acknowledgements

First of all, I would like to express my sincere gratitude to my thesis advisor Prof. Deokjung Lee of the Department of Nuclear Engineering at Ulsan National Institute of Science and Technology (UNIST). His continuous support and guidance since my undergraduate studies up until completing the master program helped in research, writing this thesis, and self-development. I could not have imagined having better advisor and mentor for my master study.

Besides my advisor, I would like to thank the rest of committee: Prof. Hyun Chul Lee at Pusan National University and Prof. Eisung Yoon at UNIST for their insightful comments, and questions which encourage me to look at my research from various perspectives.

I thank Dr. Jonghwa Chang at Korea Atomic Energy Research Institute for help in understanding the converting process of Reich-Moore resonance parameters into corresponding poles and residues.

My sincere thanks to Prof. Benoit Forget from MIT and his students Pablo Ducru and Colin Josey for help in understanding the windowed multipole representation, sharing the OpenW code and WMP library for 71 isotopes.

I would like also to thank all my fellow seniors and lab mates: Dr. Peng Zhang, Dr. Jiankay Yu, Dr. Sooyoung Choi, Dr. Taewoo Tak, Dr. Matthieu Lemaire, Dr. Alexey Cherezov, Hyunsuk Lee, Wonkyeong Kim, Jiwon Choe, Chidong Kong, Jinsu Park, Hanjoo Kim, Yunki Jo, Bamidele Ebiwonjumi, Kiho Kim, Sanggeol Jeong, Eun Jeong, Jaerim Jang, Nguyen Tung Dong Cao, Nguyen Khang Hoang Nhat, Woonghee Lee, Tuan Quoc Tran, Yongmin Jo, Lezani Van Der Merwe, Nhan Nguyen Trong Mai, Vutheam Dos, and all others for stimulating discussions, sleepless nights working together, supporting my studies and my stay in Korea.

I take this opportunity to thank all faculty members and staff in Department of Nuclear Engineering at UNIST for their help and support during my studies. Finally, I must express my very profound gratitude to my parents and elder brother for supporting me, encouraging me in all my pursuits, and inspiring me to follow my dreams. I know that my parents and brother believe in me and want the best for me. Especially, I thank my family for supporting me during my undergraduate and master course programs in South Korea. This accomplishment would not be possible without them.